Gravity wave parameters and their seasonal variations derived from Na lidar observations at 23°S

Guotao Yang,[1] Barclay Clemesha,[1] Paulo Batista,[1] and Dale Simonich[1]

Received 17 November 2005; revised 27 March 2006; accepted 12 July 2006; published 8 November 2006.

[1] The nightly and seasonal variability of gravity wave activity and spectra in the mesopause region are studied with 10 years of sodium lidar observations. From the linear layer density response to gravity wave forcing, the lidar data were analyzed to get the atmospheric density perturbations and their spectra. The atmospheric density perturbation, density variance for fluctuations with vertical scales between 2 and 10 km, and amplitudes of density perturbation spectra at m = $2\pi/8$ km and $2\pi/4$ km all exhibit large nightly variability as well as large seasonal variations, with the semiannual maxima occurring near the equinoxes. The mean RMS atmospheric density perturbation and the mean RMS horizontal wind perturbations over our site are 5.1% and 25 m/s, respectively. The growth lengths of the density perturbations in spring and autumn are lower than those in summer and winter, and the annual mean value is 38 km. The annual mean density shear variance is about 15 $(\%/km)^2$, and the maxima occur near the equinoxes. The mean Richardson number is about 1.0. The mean value of the RMS vertical wind perturbation is 0.85 m/s with a maximum occurring at the end of the year. The m spectra show power law shapes, and their range of variation is between -2.06 and -3.81 with an annual mean value of -2.93. The ω spectra also show power law shapes, and their range of variation is between -1.06 and -2.32, with an annual mean of -1.64. The mean amplitudes of density perturbation spectrum, Fa(m) (m = $2\pi/4$ km), and of the horizontal wind fluctuation, Fu(m) (m = $2\pi/4$ km), are 1.35(m/cycles) and 3×10^5(m^2 s^{-2}/(cycles/m)), respectively. The value of λ_z* averaged around autumn equinox is 14.8 km, which is lower than the value of 16.8 km, averaged around spring equinox. The annual mean of T* is 23.5 hours. The fact that the joint (m,ω) spectra are not separable, together with the large variability found in the m spectra slopes, is not compatible with linear instability theory but is compatible with Doppler spreading theories and diffusive filtering theory.

Citation: Yang, G., B. Clemesha, P. Batista, and D. Simonich (2006), Gravity wave parameters and their seasonal variations derived from Na lidar observations at 23°S, *J. Geophys. Res.*, *111*, D21107, doi:10.1029/2005JD006900.

1. Introduction

[2] Gravity waves have great influence on the circulation, structure and composition of the middle and upper atmosphere. In the past, many observations of gravity wave phenomena have been carried out by remote sensing techniques such as airglow observations, radar and lidar. The sodium lidar is a useful tool for studying gravity wave activity and spectra in the mesopause region, especially at high frequencies and high wave numbers, as lidar has high temporal and spatial resolutions of a few minutes and a few hundred meters, respectively. Moreover, the sodium layer is a good tracer of gravity wave perturbations because the steep sodium density gradients on the bottom and topsides of the layer enhance the wave perturbations. Using sodium lidar observational data, several studies of gravity wave intensities, spectra and wavefield characteristics in the mesopause region have been made [e.g., *Senft and Gardner*, 1991; *Collins et al.*, 1994; *Manson et al.*, 1998].

[3] Many theoretical studies of gravity waves have also been made, most of which have concentrated on explaining the vertical wave number spectrum, after *Vanzandt* [1982] found there may exists a "universal" atmospheric spectrum similar to the oceanic spectrum. The first widely applied theory was *Dewan and Good*'s [1986] linear instability theory. Later, however, several other theories based upon different fundamental physics were also developed, such as the Doppler-spreading theory [*Hines*, 1991], the saturated-cascade theory [*Dewan*, 1994], and the diffusive filtering theory [*Gardner*, 1994].

[4] While many observations have been carried out for only a few hours or days, the study of seasonal variations in gravity wave activity needs months or years of observations. Observations of this sort have been carried out, providing information on the seasonal variation of gravity wave activity in the middle and upper atmosphere. A solstice maximum is present in most observations, while the annual component is

[1]Instituto Nacional de Pesquisas Espaciais, São José dos Campos, Brazil.

0148-0227/06/2005JD006900

dominant in the stratosphere, but a semiannual oscillation is observed in the mesosphere and lower thermosphere (see the review by *Fritts and Alexander* [2003]). However, some workers have reported slightly different behavior; *Gavrilov et al.* [2003] reported maximum gravity wave intensities at the solstices below 83 km, with a shift to the equinoxes at higher altitudes for Hawaii (22°N, 160°W), and *Gavrilov and Jacobi* [2004] found the gravity wave perturbations to be a maximum at the solstices near 83 km, shifting to equinox near and above 100 km for Collm, Germany (52°N, 15°E).

[5] In this paper, we present a comprehensive report on gravity wave parameters derived from sodium lidar measurements made at a southern low-latitude location, São José do Campos (23°S, 46°W), on the basis of many years of observational data. We present the seasonal variations of the gravity wave activity and spectra. We also report the seasonal variability of some other characteristics of the gravity wave field, such as Richardson's number, vertical wind perturbations, and characteristic wavelength and period. We also compare our results with the predictions of theories of gravity wave saturation and dissipation. In our analysis we have used the techniques first described by *Senft and Gardner* [1991], and we have retained the same terminology as these workers. The paper is organized in sections as follows. After a brief description of the observation in section 2, we describe the data analysis methods and the results for the seasonal variations of gravity wave activity and spectra in section 3. The first part of this section is a general introduction to the data analysis methods for obtaining the atmospheric parameters reported in this paper. The second part describes the results for the seasonal variability of the total density perturbation, growth length of the density perturbation, vertical shear variance, vertical wind perturbations, and the separability of the joint (m, ω) spectrum. In the third part, the seasonal variations of the m spectra amplitudes and slope index, and the characteristic vertical wavelength are presented. The seasonal variations of the ω spectra amplitudes and slope index, and the characteristic period are given in the last part. In Section 4, we discuss the seasonal variation of the gravity wave activity over our site and give some possible explanations. We compare our results for the characteristics of the gravity wave field to the results of other lidar observations and discuss the reasons for differences between them. We also compare our results to the predictions of gravity wave theories. Finally, a summary of the results presented in this paper is made in section 5.

2. Observations

[6] Our sodium lidar measurement technique and the precision of measurement have been described in our earlier papers [e.g., *Simonich et al.*, 1979; *Clemesha et al.*, 1992]. Here, following *Senft and Gardner* [1991] we introduce a parameter σ_a^2 which is determined by the lidar detection capability and is used to calculate the errors in the gravity wave analysis. σ_a^2 is the photon noise bias and is defined as

$$\sigma_a^2 = \frac{4\Delta z \Delta t}{\lambda_c T_c} \frac{\mu^2}{TL} \int_{z_0-L/2}^{z_0+L/2} \int_{t_0-T/2}^{t_0+T/2} \frac{dtdz}{N_s(z,t)} \qquad (1)$$

where

μ^2 ~ 0.024 is a scale factor;
Δz altitude resolution of the sodium profile (m);
Δt time resolution of the sodium profile (s);
λ_c low-pass filter cutoff vertical wavelength (m);
T_c low-pass filter cutoff temporal period (s);
L altitude range of observations (m), $\approx$20 km;
T observation period (s);
z_0 sodium layer centroid height (m);
$N_s(z, t)$ sodium photon count at altitude z and time t.

[7] σ_a^2 is inversely related to the signal level N_s, so it is mainly decided by the lidar power–aperture product and the atmospheric transmittance. If the cutoffs of the filter are 2π/(1.5 km) and 2π/(20 min), the σ_a^2 of our lidar is about 7×10^{-5}, which is close to the value of the UIUC lidar (5×10^{-5} for the same T_c and λ_c) used by *Senft and Gardner* [1991], but is much higher than the value of 5×10^{-6} for the more powerful CEDAR lidar, also used by the Illinois workers.

[8] Our sodium lidar, which has been used to observe the sodium layer for more than 30 years, has an altitude resolution of 250 m or 300 m, and time resolution of 3 min or 5 min. We selected the data from 1994 to 2004 for calculating the characteristics of the gravity wave field reported in this paper. These data include a total of 82 suitable nights of observations, and the data on some nights consist of about 3 hours of continuous observation with good signal levels, while the observation time on the other nights is longer than 3 hours. As sporadic sodium layers (N_s) and the production and loss of sodium atoms, obviously not caused by the gravity waves, are common in our lidar data [*Batista et al.*, 1989], we frequently have to discard stretches of data, and only occasionally do we have useful data sequences longer than 3 hours.

3. Data Analysis and Results

3.1. General Introduction to the Data Analysis

[9] The perturbations in the atmospheric winds, temperature, and density induced by the gravity waves are customarily used to describe gravity wave activity. However, we cannot see the perturbations in atmospheric density or winds directly from the sodium lidar data, rather we get the sodium density perturbations, which need to be transformed into atmospheric density perturbations. Only considering the linear effects, *Senft and Gardner* [1991] give a relation between the perturbations of the sodium density and the atmospheric density

$$rs(z,t) = -\frac{1}{\gamma - 1}\left[1 - \frac{\gamma H(z - z_0)}{\sigma_o^2}\right] ra(z,t) \qquad (2)$$

where rs(z, t) is the sodium density perturbation; ra(z, t) is the atmospheric density perturbations; and σ_0 is the RMS thickness of the unperturbed sodium layer ($\sim$4.5 km).

[10] We first get the atmospheric density fluctuations ra(z, t) from the above relation and then use them to obtain the parameters of the atmospheric density perturbations and spectra. When we do this we can see that the absolute value of the term in square brackets |Sca(z)| (here, we use Sca(z) to denote $[1-\gamma H(z-z0)/\sigma_0^2]$) in equation (2) will go to zero

near the height z1 = z0 + σ_0^2/γH ~ 94 km, and this means the first-order wave effects have no influence on the sodium profile in this height. As a result of this it is not possible to get a reliable value of ra(z,t) from rs(z,t) within ±2 km of z1 [*Senft and Gardner*, 1991]. So we have to discard some data points where |Sca(z)| is too small.

[11] To obtain r_s(z, t), we must know the form of the unperturbed sodium layer. *Senft and Gardner* [1991] use a Gaussian as the unperturbed sodium layer. They also stipulated a criterion: if the unperturbed sodium layer is modeled as ρ_0(z) = A exp[−f(z)], where

$$f(z) = \frac{(z-z0)^2}{2\sigma_o^2} + \frac{f^{(3)}(z_0)}{3!}(z-z0)^3 + \sum_{n=4}^{\infty}\frac{f^{(n)}(z_0)}{n!}(z-z0)^n \quad (3)$$

if the error of the Gaussian model for the unperturbed sodium layer is mainly contributed to by the second term on the right hand side of equation (3), the Gaussian model will be valid provided:

$$\frac{f^{(3)}(z_0)}{3!}\left(\frac{L}{2}\right)^3 \ll 1.1 \quad (4)$$

[12] However, in our data, the left hand side of (4) for the average sodium layer on most nights is ~1, so we average the observational sodium data temporally and spatially (whole night and 6 km average) instead of using a Gaussian shape. The relation between ra(z, t) and rs(z, t) then becomes

$$ra(z,t) = -\frac{\gamma-1}{1-\gamma H f'(z)} rs(z,t) \quad (5)$$

where f′(z) = $-\rho_0$(z)/ρ_0′ (z). In practice, we use numerical calculation to obtain ρ_0′(z) and f′(z) on the basis of the unperturbed sodium layer shape, ρ_0(z).

[13] Again following *Senft and Gardner* [1991] the horizontal wind perturbations and fluctuations spectra can be related to the atmospheric density perturbations by using the following equations:

$$\langle u'^2\rangle = \left(\frac{g}{N}\right)^2 \langle ra^2\rangle \quad (6)$$

$$Fu(\omega) = \left(\frac{g}{N}\right)^2 Fa(\omega) \quad (7)$$

$$Fu(m) = \left(\frac{g}{N}\right)^2 Fa(m) \quad (8)$$

where $\langle u'^2\rangle$ and $\langle ra^2\rangle$ are the mean squared horizontal wind and atmospheric density perturbations, respectively. Fa(ω) and Fa(m) are the atmospheric density perturbation spectra, and Fu(ω) and Fu(m) are for the horizontal wind, g is the acceleration due to gravity and N is the Brunt-Vaisala frequency defined as $N^2 = g/T_{em}[dT_{em}/dz + g/Cp]$, where T_{em} is atmospheric temperature and Cp is specific heat at constant pressure. In this paper, we use a fixed value N = 0.0196 rad/s from lidar observations of temperature in the mesopause region over our site [*Clemesha et al.*, 1999], making the factor $(g/N)^2$ equal to 23.5 × 10^4 $(m/s)^2$ which is 15% higher than that used by *Senft and Gardner* [1991].

[14] The errors caused by photon noise for the atmospheric parameters reported in this paper are given in Table 1. The errors are estimated using the methods of *Senft and Gardner* [1991, Table B1]. The relative RMS errors of atmospheric parameters are not higher than 13%, except in the cases of the RMS vertical winds (20%) and vertical wave number spectrum amplitude at m = 2π/2.5 km (18%). The reason that the errors of temporal frequency spectrum and slope are not very high is that the calculation of the temporal frequency spectrum is based on two night averages.

3.2. Atmospheric Density Perturbations

[15] The mean square atmospheric density perturbations are obtained by averaging ra^2(z, t) over time and altitude:

$$\langle ra^2(t)\rangle = \frac{1}{TL'}\int_{z_0-L/2}^{z_0+L/2}\int_{t-T/2}^{t+T/2} ra^2(z,\tau)\,d\tau\,dz \quad (9)$$

[16] L′ is the altitude range where |Sca(z)| is not too small $(Sca(z)^2 > 0.5)$, which will generally lead to discarding data points within about ±2.5 km of z1. The sodium density profiles were first low-pass filtered temporally and spatially with cutoffs of 2π/30 min and 2π/2 km (to decrease the errors in the vertical shear variance and the temporal derivative variance, we have to increase the cutoff period and wavelength of the filter). The temporal variations of $\langle r_a^2\rangle$ were then computed by averaging r_a^2 throughout the sodium layer over a period of T = 2 hours (here we make T = 2 hours to facilitate comparison with *Senft and Gardner*'s [1991] results).

[17] The seasonal variation of the RMS atmospheric density perturbations is shown in Figure 1. The range of the density perturbations during each night and its average

Table 1. Errors Caused by Photon Noise for the Atmospheric Parameters Reported in This Paper

Parameter	Symbol	Relative RMS Error, %
Atmospheric density variance	$\langle ra^2\rangle$	2.4
Vertical shear variance	$\langle(\partial ra/\partial z)^2\rangle$	5.7
Temporal derivative variance	$\langle(\partial ra/\partial z)^2\rangle$	7.4
RMS horizontal winds	$\langle u'^2\rangle^{1/2}$	10
RMS vertical winds	$\langle w'^2\rangle^{1/2}$	20
Vertical and temporal derivative variance	$\langle(\partial^2 ra/\partial z\partial t)^2\rangle$	11
RMS vertical wavelength	λ_{zrms}	3.1
RMS period	T_{rms}	3.8
B_{rms}	B_{rms}	5.7
Characteristic vertical wavelength	λ_z^*	4.5
Characteristic period	T*	13
Vertical wave number spectrum	Fa(m) at $m_8 = 2\pi/8$ km	3.7
	$m_4 = 2\pi/4$ km	8.0
	$m_{25} = 2\pi/2.5$ km	18
Temporal frequency spectrum	Fa(ω) at $\omega_1 = 2\pi/60$ min	5.0
	$\omega_2 = 2\pi/40$ min	7.4
	$\omega_3 = 2\pi/25$ min	11
Frequency spectral slope	p	<10
Wave number spectral slope	q	<13

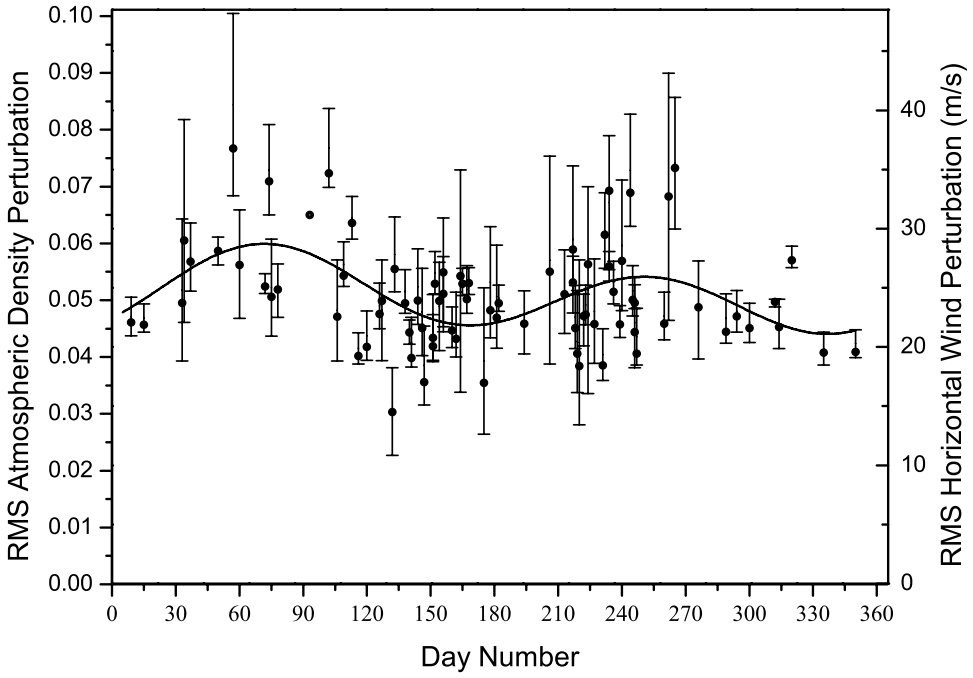

Figure 1. Seasonal variations of the RMS atmospheric density perturbations. The dots denote nightly average density perturbations, and the lines represent the range of variation during the night. The solid curve is MMSE fit to the atmospheric density perturbation for the mean, annual, and semiannual components. The data are scaled for RMS horizontal wind perturbation on the right-hand axis.

are both shown. These perturbations are induced by gravity waves with periods between 30 min and ~4 hours, and vertical wavelengths between 2 km and ~40 km. A MMSE (minimum mean square error) fit was made after interpolation as our data are not uniformly distributed throughout the year, and the fit parameters and their uncertainties are shown in Table 2. In Table 2, u1 (u2) denotes the uncertainty of the amplitude A1 (A2) while ud1 (ud2) denotes that for d1 (d2). Here, we use the uncertainties (u1 or u2) of the amplitudes (A1 or A2) to compare to the amplitudes (A1 or A2) as the criterion for whether an annual or semiannual variation is significant. We categorize an annual (semiannual) variation as significant when u1/A1 (u2/A2) is lower than 30%, moderately significant when u1/A1 (u2/A2) is between 30% ~ 40%, weakly significant when u1/A1 (u2/A2) is between 40% and 50%, and insignificant when u1/A1 (ud/A2) is higher than 50%. The semiannual uncertainty (u1/A1) in Figure 1 is only 20%, indicating that the semiannual variation of the density perturbations is significant, and the annual variation is not insignificant as u2/A2 is 42%. The annual mean value of the RMS atmospheric density perturbations is 5.1% and the maximum is near March (5.8%). This means the strongest gravity wave activity (waves from 2 km to 40 km and 30 min to 4 hours) occurs in early March. The semiannual component (0.6%) is more prominent than the annual component (0.3%), with the semiannual and annual components being 12% and 6% of the annual mean component, respectively. The magnitudes of the perturbations in March and September are obviously higher than those in December and June, indicating equinoctial maxima in gravity wave activity at our location. The right-hand axis in Figure 1 is the RMS horizontal wind perturbations, which are obtained by multiplying by a factor $(g/N)^2$ (equation (6)). So the wind perturbations have the same seasonal variation as the atmospheric density perturbations and an annual mean value of 25 m/s.

[18] The amplitude growth characteristics of the gravity wave field can be investigated, by computing the mean square values of ra(z,t) at each height:

$$\langle ra^2(z)\rangle \cong \frac{(\gamma-1)^2}{[1-\gamma Hf'(z)]^2}\frac{1}{T}\int_0^T [rs(z,t)-\overline{rs}(z)]^2 dt \qquad (10)$$

where

$$\overline{rs}(z)=\frac{1}{T}\int_0^T rs(z,t)dt \qquad (11)$$

[19] The sodium density profiles are first low-pass filtered with 30 min and 2 km cutoffs as before, then $\langle ra^2(z)\rangle$ at each height is obtained. Because the maxima of gravity wave activity occur in March and September, we define autumn, winter, spring and summer, as consisting of months (2, 3, 4), (5, 6, 7), (8, 9, 10), and (11, 12, 1), respectively.

[20] Figure 2 shows how $\langle ra^2(z)\rangle$ varies with height in the four seasons. An exponential curve (dotted line) is fitted in a least mean squares sense to obtain the amplitude growth of the density perturbations with height. It can be seen that the density perturbations are about 4% near 80 km in all the four seasons, and that the perturbations increase to 8% at the top of the sodium layer in spring and autumn, and 6% in winter and

Table 2. Annual and Semiannual Components of Gravity Wave Parameters[a]

	A0	A1	A2	d1	d2	u1	u2	ud1	ud2	u1/A1	u2/2
$\langle ra^2\rangle^{1/2}$, %	5.1	0.3	0.6	85	70	0.127	0.122	25.6	6.9	0.42	0.20
$\langle(\partial ra/\partial z)^2\rangle$, (%/km)^2	15	2.9	4.8	100	75	1.24	1.25	26.9	7.3	0.43	0.26
$\langle(\partial ra/\partial t)^2\rangle$, (%/hours)^2	12.4	1.5	0.4	25	145	0.508	0.46	21.2	35.8	0.34	1.15
q	−2.96	0.11	0.16	315	10	7.3e−3	8.3e−3	41	13	0.67	0.52
E_m, (%)^2	7.2	1.1	1.7	85	70	0.55	0.53	29.6	10.2	0.5	0.31
Fa(m_8), m/cycles	6.4	1.4	2.4	125	80	0.686	0.704	32.3	9.4	0.49	0.29
Fa(m_4, m/cycles	1.36	0.28	0.17	30	65	0.109	0.102	23.6	20.4	0.39	0.60
Fa(m_{25}, m/cycles	0.27	0.06	0.02	40	30	0.025	0.025	24.9	41.5	0.415	1.26
λ_z^*, km	15.8	2.2	0.1	270	20	0.850	0.832	22.5	249	0.39	8.3
p	−1.66	0.18	0.02	215	65	0.073	0.059	24.6	115	0.41	2.97
Fa(ω_1), s/cycles	0.62	0.23	0.15	25	40	0.081	0.081	23.8	16.7	0.35	0.54
Fa(ω_2), s/cycles	0.29	0.07	0.02	350	50	0.022	0.022	19.2	33.1	0.32	1.09
Fa(ω_3), s/cycles	0.13	0.02	0.02	10	30	0.014	0.016	45.5	24.1	0.72	0.82
T*, hours	22.2	4.6	3.2	145	50	2.88	2.55	38.7	23.9	0.63	0.80

[a]Gravity wave parameters are $\hat{y}$ = A0 +A1 cos[2π/365(d−d1)] +A2 cos[4π/365(d−d2)].

summer. So their growth lengths are also different. The growth lengths in summer and winter (59 km and 41 km) are higher than those in spring and autumn (34 km and 26 km), which means that the density perturbations increase more rapidly with height in spring and autumn than in summer and winter. The growth lengths in the four seasons are all greater than the value expected for unsaturated waves, 2H ≈ 12 km. This indicates that gravity waves in the upper mesosphere at our location are damped during all four seasons, but more in summer and winter than spring and autumn.

[21] The annual mean growth length of the density perturbations obtained by us is 38 km, which is lower than the value of 54 km reported by *Senft and Gardner* [1991], but is higher than the 25 km reported by *Vincent and Fritts* [1987] for Adelaide. A lower value, 10 km, reported by *Beatty et al.* [1992] for Arecibo Observatory (18°N, 67°W) is comparable with the theoretical growth length of 12 km for unsaturated waves.

[22] The dynamic stability of the wavefield can be characterized by the vertical shear of the horizontal wind

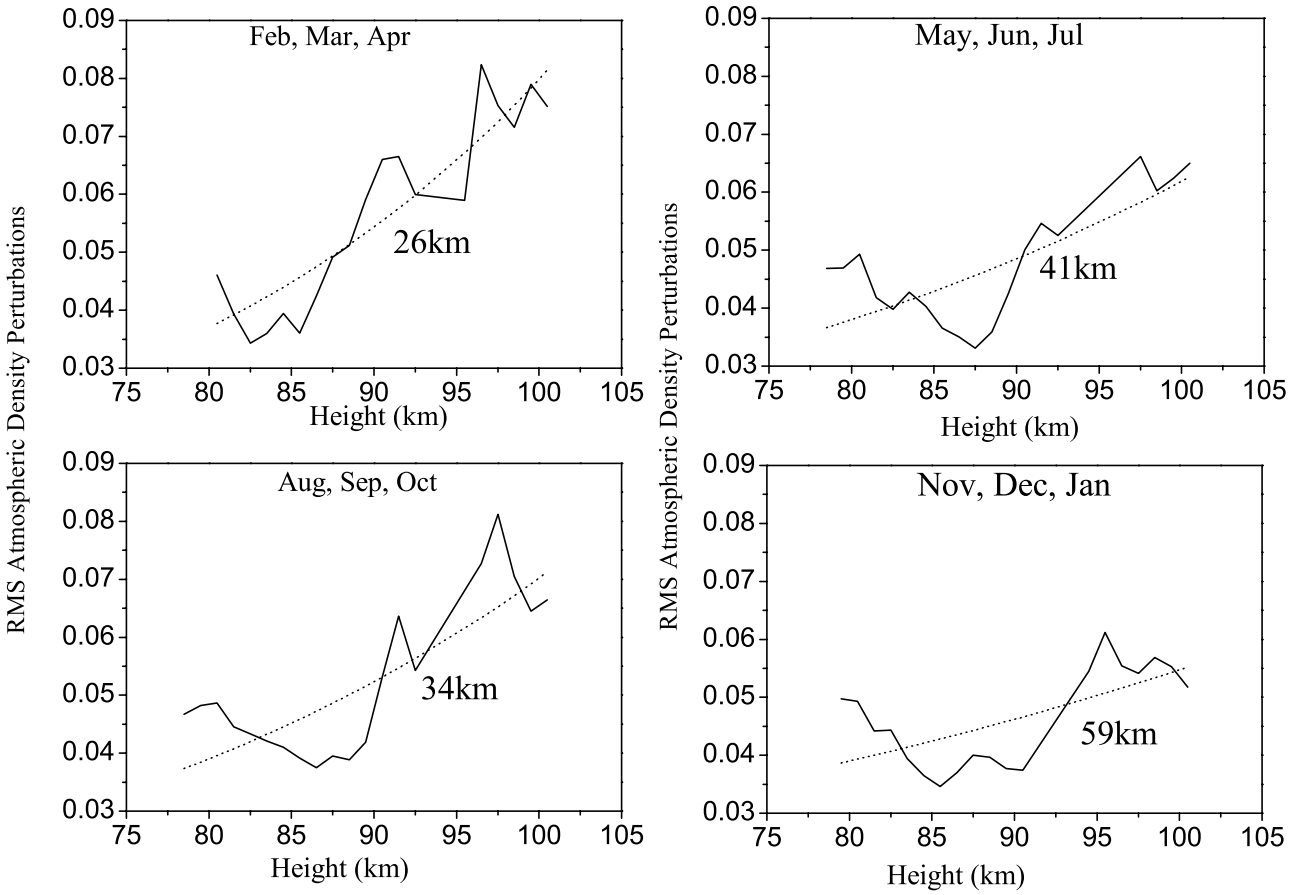

Figure 2. Mean profiles of the RMS atmospheric density perturbations in different seasons versus height. The dotted exponential curves are the least squares fits, and their growth lengths are also marked.

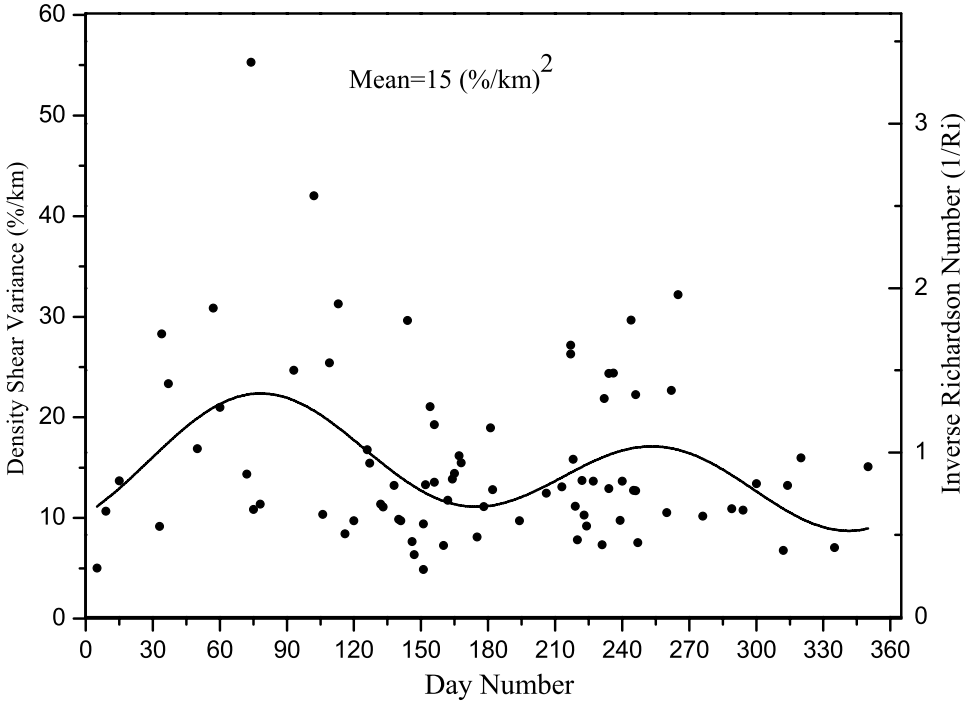

Figure 3. Seasonal distribution of density vertical shear variance. The solid curve is the MMSE fit. The data are scaled for inverse Richardson number (Ri) on the right-hand axis.

perturbations and the Richardson number. These two parameters can be obtained from the atmospheric density shear variance [*Senft and Gardner*, 1991]:

$$Ri = \frac{N^2}{\langle \left(\frac{\partial u'}{\partial z}\right)^2 \rangle} \cong \frac{N^4}{g^2 \langle \left(\frac{\partial r_a}{\partial z}\right)^2 \rangle} \tag{12}$$

[23] The atmospheric density shear variance is directly obtained from the density perturbations ra(z,t), obtained from equation (5). Here again, some data points near z1 have not been used. The sodium density was also filtered with cutoffs of $2\pi/30$ min and $2\pi/2$ km. The seasonal distribution of the density shear variance is given in Figure 3. A MMSE fit for the mean, annual and semiannual components was made as before. The annual mean density shear variance is about 15 $(\%/\mathrm{km})^2$ and the mean Richardson number is about 1.0. A weak annual variation is present and the semiannual variation is significant. The annual and the semiannual components are 20% and 32% of the annual mean value, respectively. The semiannual maxima are near the equinoxes, like the total density perturbations, but different to the behavior reported by *Senft and Gardner* [1991], who found maxima around the solstices. For most of the year, Ri is in the range of 0.5 to 2.

[24] The vertical wind perturbations can be obtained from the temporal derivative variance of the density perturbations, neglecting the second term on the right hand side.

$$\begin{aligned} \frac{g^2}{N^4} \langle \left(\frac{\partial r_a}{\partial t}\right)^2 \rangle &= \langle w'^2 \rangle + \frac{\overline{u}^2}{N^2} \langle \left(\frac{\partial u'^2}{\partial x}\right)^2 \rangle \\ &= \langle w'^2 \rangle + \frac{\overline{u}^2}{N^2} \langle u'^2 \rangle k_{rms}^2 \end{aligned} \tag{13}$$

[25] The sodium data are again filtered with cutoffs corresponding to 30 min and 2 km and the result is given in Figure 4. Shown in Figure 4 is the seasonal distribution of RMS vertical wind perturbations w'_{rms}. A MMSE fit was also made. The seasonal variation can be considered to be present as the annual uncertainty (ud1) is 34%. The annual mean value of the RMS vertical wind perturbations is 0.85 m/s and the relative annual amplitude is 12%. The maximum occurs at the end of the year, unlike that of the density perturbations and vertical shear variance.

[26] If we assume that the ratio between the horizontal and vertical path lengths between the sources and our site is equal to: $\frac{u'_{rms}}{w'_{rms}}$, which is

$$\frac{u'_{rms}}{w'_{rms}} = \frac{\sqrt{\left(\frac{g}{N}\right)^2 \langle r_a^2 \rangle}}{\sqrt{\frac{g^2}{N^4} \langle \left(\frac{\partial r_a}{\partial t}\right)^2 \rangle}} \tag{14}$$

[27] We can get the horizontal distance between the source and our site provided the vertical distance is known. Assuming the sources are in the troposphere, about 90 km below the sodium layer, makes them about 2700 km away from our location. The Andes are about 2200 km from our site and taking into consideration the fact that the high-frequency cutoff of our filter will have little effect to increase the distance, it is reasonable to suggest that mountain waves generated by the Andes might be one of the principal sources of the gravity waves detected by our lidar.

[28] *Senft and Gardner* [1991] used a simple method to test the separability of the joint (m, ω) spectrum Fa(m, ω).

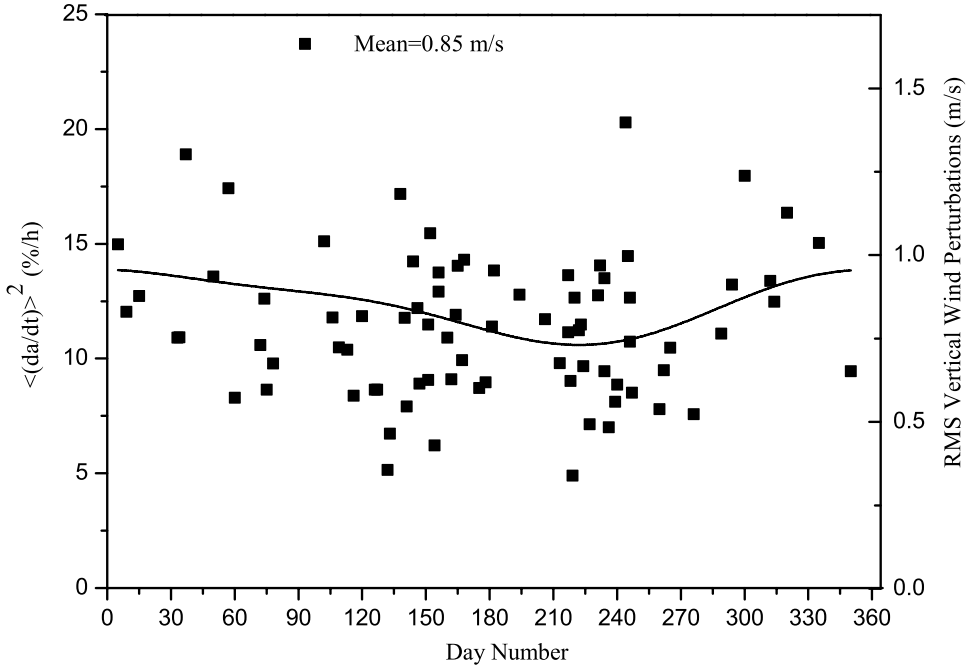

Figure 4. Seasonal distribution of RMS vertical wind perturbations w'_{rms}. The data are scaled for vertical wind on the right-hand axis.

The following equations must be satisfied if the joint (m,ω) spectrum Fa(m, ω) is separable:

$$B^2_{rms} = \frac{\int_0^{m_b}\int_f^N m^2\omega^2 Fa(m,\omega)d\omega dm}{\int_0^{m_b}\int_f^N Fa(m,\omega)d\omega dm} = m^2_{rms}\omega^2_{rms} \qquad (15)$$

or

$$B^2_{rms} = \frac{\left\langle\left(\frac{\partial^2 r_a}{\partial z\partial t}\right)^2\right\rangle}{\langle r_a^2\rangle} = \frac{\left\langle\left(\frac{\partial r_a}{\partial z}\right)^2\right\rangle\left\langle\left(\frac{\partial r_a}{\partial t}\right)^2\right\rangle}{\langle r_a^2\rangle\langle r_a^2\rangle} \qquad (16)$$

[29] Equation (16) can be used to test for separability of the joint (m, ω) spectrum Fa(m, ω). To decrease the photon noise bias to $\langle(\partial^2 ra/\partial z\partial t)^2\rangle$, the sodium data were low-pass filtered with cutoffs of $2\pi/4$ km and $2\pi/40$ min. Then B^2_{rms} was obtained with compensation for photon noise bias.

[30] B_{rms} is plotted versus $m_{rms}\omega_{rms}$ in Figure 5. If Fa(m, ω) can be separated, the data points in Figure 5 should lie on the line: $B_{rms} = m_{rms}\omega_{rms}$. However, from Figure 5, we can see that data points are highly scattered and a least mean square fit to the data is $B_{rms} = 1.7 \times 10^{-9} + 0.48(m_{rms}\omega_{rms})$, indicating that the joint (m, ω) Fa(m, ω) cannot be separated.

3.3. Vertical Wave Number Power Spectra of the Atmospheric Density Perturbations

[31] The vertical wave number power spectrum Fa(m) of the atmospheric density perturbations gives the contribution of gravity waves with different vertical wavelengths to the density perturbations. It can be obtained by the spatial Fourier transform of the autocorrelation function of the atmospheric density perturbations:

$$Fa(m) = \int_{-\infty}^{+\infty} Ba(s,0)e^{ims}ds \qquad (17)$$

[32] Here, Ba(s, 0), the autocorrelation function of the atmospheric density perturbations, is equal to $\langle$ra(z, t)ra(z−s, t)$\rangle$. Since the autocorrelation function can be computed without interpolating missing data points, this method of computing the power spectrum is most convenient for our data, which has a large gap (∼5 km) in the atmospheric density perturbations.

[33] As in the work by *Tsuda et al.* [1989], we first prewhiten the density perturbations $r_a(z, t)$: $y(z, t) = r_a(z, t) - 0.95r_a(z-\Delta z, t)$, then calculate the vertical correlation function of y(z, t), and use a Hanning window to suppress end effects due to the finite length of the data series. After the Fourier transform, Fa(m) is obtained after compensating for prewhitening by using a recoloring process. The sodium data are temporally low-pass filtered with a 20 min filter. The Fa(m) for each night is obtained by arithmetically averaging Fa(m) from each single data profile. Note that the photon noise floor must be estimated and subtracted from the average spectrum.

[34] In Figure 6 we show four examples of the vertical wave number power spectra of the atmospheric density perturbations for four different nights. The data are plotted as single-sided spectra of atmospheric density perturbations in units of m/cycles. A linear regression fit to the spectra for vertical wavelengths from 1.5 km to 8 km is also shown in

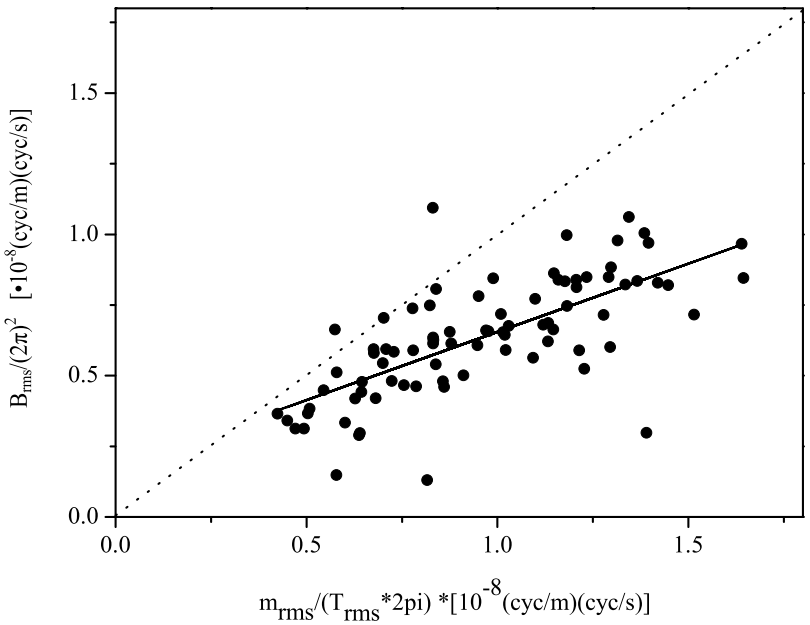

Figure 5. B_{rms} versus $m_{rms}\omega_{rms}$. The solid line is the least mean square fit to the data [$B_{rms} = 1.7 \times 10^{-9} + 0.48(m_{rms}\omega_{rms})$].

the graphs. The horizontal wind spectrum Fu(m) can be obtained by multiplying the density spectrum by $(g/N)^2$ according to equation (8). Comparing our spectra to those shown by *Senft and Gardner* [1991, Figure 13], the deviation of our spectral slope is higher than theirs. The main reason for this is that σ_a^2 (7×10^{-5}) for our sodium lidar data is 14 times higher than for the examples given by them (5×10^{-6} for the CEDAR lidar).

[35] The annual mean vertical wave number spectrum is given in Figure 7. A straight line fit to this spectrum gives a

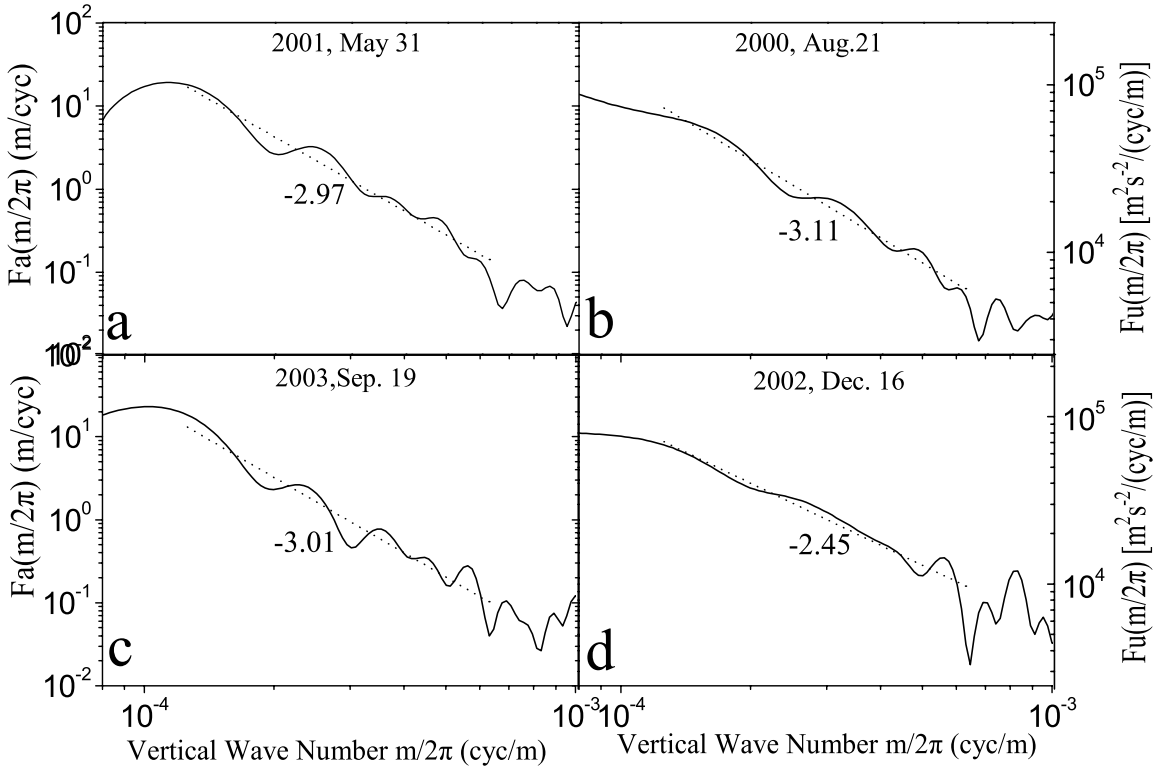

Figure 6. Vertical wave number power spectra of atmospheric density perturbations associated with gravity waves in the mesopause region. The spectra were inferred from sodium data for the nights of (a) 31 May 2001, (b) 21 August 2000, (c) 19 September 2003, and (d) 16 December 2002. The straight dotted lines are the regression fits to the spectra for vertical wavelengths from 1.5 to 8 km.

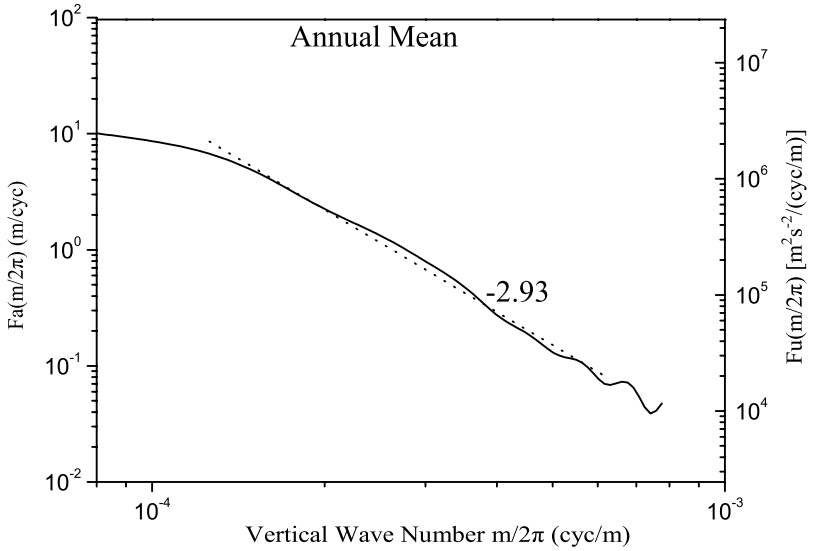

Figure 7. Vertical wave number spectra averaged for all 82 observation nights.

slope of −2.93, close to the value of −3 predicted by both the linear instability theory [*Dewan and Good*, 1986] and by the Doppler-spreading theory of *Hines* [1991]. The scale for the horizontal wind spectrum has also been marked on the right hand vertical axis. The amplitude of Fa(m) (m = 2π/4 km) is 1.35 (m/cycle) and the amplitude of Fu(m) (m = 2π/4 km) is $3*10^5$ (m^2s^{-2}/(cycles/m)), comparable to the values predicted by the models [e.g., *Dewan and Good*, 1986; *Hines*, 1991].

[36] The seasonal distribution of vertical wave number spectral slopes (q) is plotted in Figure 8. The shallowest slope is −2.06 and the steepest is −3.81. Comparing to the slopes reported by *Senft and Gardner* [1991], −2.20 and −3.55 respectively, their range of variation is slightly less than ours. The shallowest slope reported by *Senft et al.* [1993] is −2.1, which is near our value, and their steepest slope is −3.5, which is lower than ours, but their result was based on only one month of data. A range of slopes from −2.0 to −3.5 was reported by *Collins et al.* [1994] at the South Pole.

[37] No significant seasonal variation of the Fu(m) slopes can be detected as u1/A1 and u2/A2 are both higher than 50%, in agreement with the findings of *Senft and Gardner* [1991]. The slope varies greatly from day to day in our results, again in agreement with other lidar observations [*Senft and Gardner*, 1991; *Senft et al.*, 1993; *Collins et al.*, 1994].

[38] The amplitude of Fa(m) for wavelengths lower than 10 km can be considered reliable for a sodium layer width ∼20 km. The atmospheric density variance, E_m, induced by gravity waves with wavelengths between 2 km and 10 km can be obtained by integrating Fa(m) over this range. The seasonal distribution of density variance E_m (2 km to 10 km) is shown in Figure 9. The largest value is 24(%)^2 and the

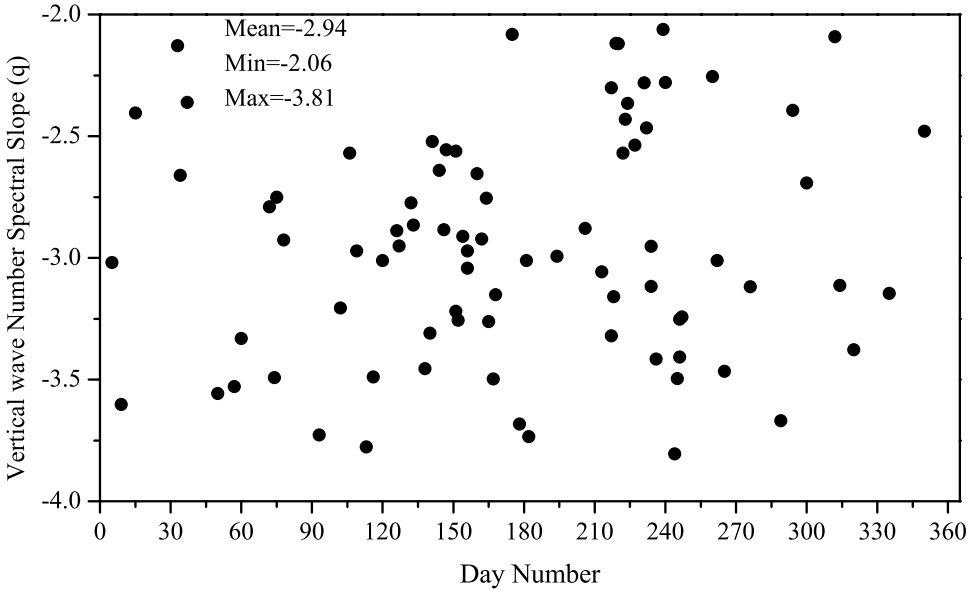

Figure 8. Seasonal distribution of power law slopes of the vertical wave number spectra.

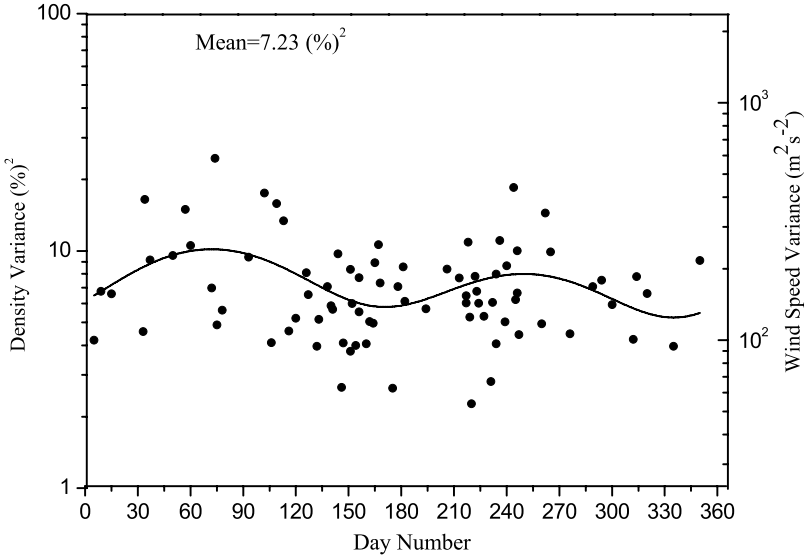

Figure 9. Seasonal distribution of density perturbation variance for fluctuations with vertical scales between 2 and 10 km.

smallest is 2.3(%)^2. Like the RMS total density perturbations shown in Figure 1, the maximum of E_m occurs in March and strong semiannual variations is present. A MMSE fit was made as before, the parameters of which are shown in Table 2. The annual mean of E_m is 7.2(%)^2, which is 36% of the total wave variance and half of that reported by *Senft and Gardner* [1991]. The semiannual and the annual components are respectively 24% and 15% of the annual mean component, and the difference between their phases is only half a month. The semiannual maxima are near the equinoxes like the total density perturbation, but the relative amplitudes of the semiannual and the annual components are higher than those of the total density perturbation.

[39] The seasonal variations of Fa(m) for $m_8 = 2\pi/(8\text{ km})$, $m_4 = 2\pi/(4\text{ km})$ and $m_{25} = 2\pi/(2.5\text{ km})$ are shown in Figure 10. From Figure 10 and Table 2, we can see that the annual mean value of m_8 is 6.4 (m/cycle), which is 55% of that reported by Senft and Gardner. Its annual variation exists and the semiannual variation is significant. The maxima occur near the equinoxes as for the total

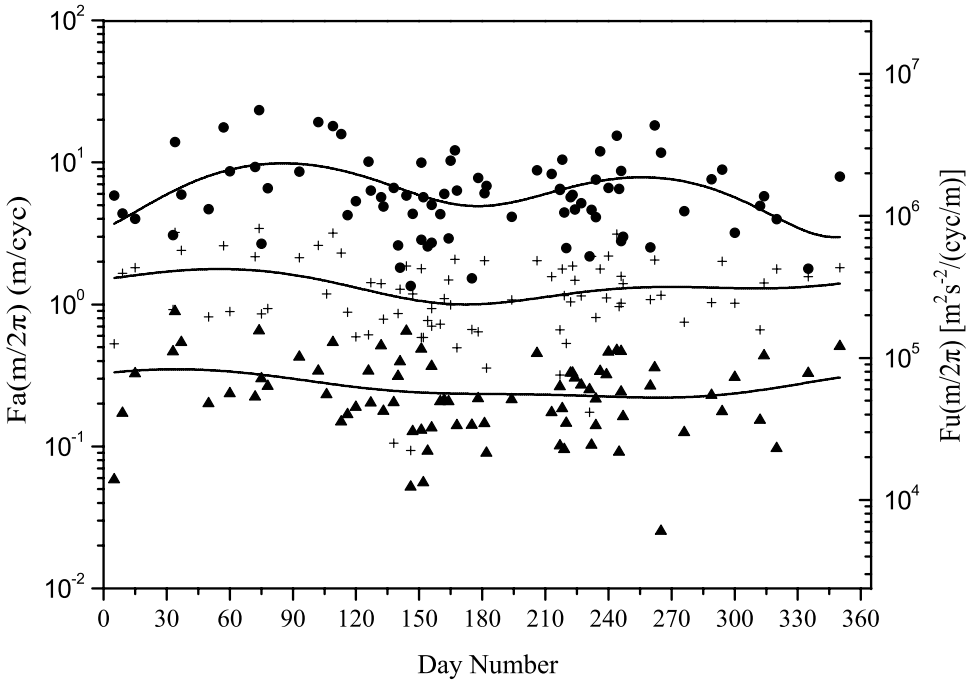

Figure 10. Seasonal distributions of vertical wave number spectral amplitudes at $m_8 = 2\pi/(8\text{ km})$ (circles), $m_4 = 2\pi/(4\text{ km})$ (pluses), and $m_{25} = 2\pi/(2.5\text{ km})$ (triangles). The solid curves are the MMSE fits for the mean, annual, and semiannual components.

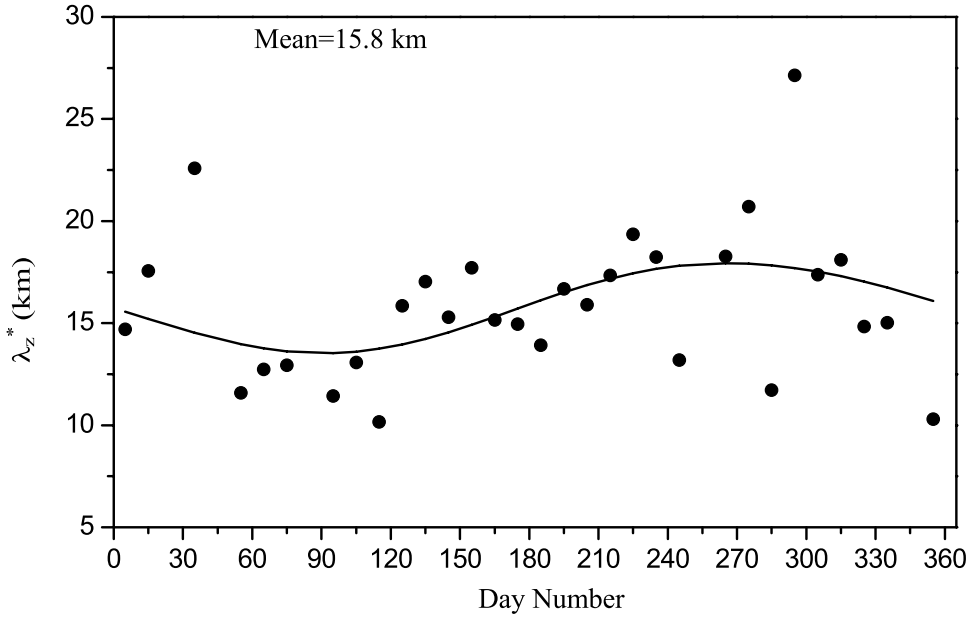

Figure 11. Seasonal distributions of characteristic vertical wavelength. The solid curve is the MMSE fit.

density perturbation and E_m. The annual and the semiannual components are respectively 22% and 38% of the annual mean value, and their phases are both near the equinoxes. The annual mean of m_4 is 1.36 (m/cycles) and the relative amplitude of the semiannual component is not as strong as that of E_m and m_8, only 13%. Although the maximum occurs near March and the phase of the semiannual oscillation corresponds to peaks near the equinoxes, the value in summer is comparable to that in spring. The relative amplitude of the annual variation is 21%, the same as m_8, and its time of maximum shifts to day 30. The annual mean of m_{25} is 0.27, and the annual component of m_{25} is 0.06. The annual component of m_{25} is 22% of the annual mean value, and the phases of the annual components shift to give a maximum in February. The relative amplitudes of the annual components of m_8, m_4, and m_{25} are all about 22%, which is much higher than that of the total density perturbation.

[40] The characteristic vertical wavelength λ_z^* defines the breakpoint between the weak and strong wave interaction subranges and, following *Senft and Gardner* [1991],

$$m_* = \left[\frac{\eta m^q Fa(m)}{2\pi\langle r_a^2\rangle}\right]^{\frac{1}{q-1}} \tag{18}$$

[41] From equation (18) we can see that m* is very sensitive to the spectral slope and the value Fa(m = 2π/4 km). Because the bias of the photon noise of our data is considerably larger than that of *Senft and Gardner* [1991] it was necessary to average. To do this we divided the year into 37 intervals of just under 10 days, typically containing 1–3 nights each. The averaged spectra for these intervals were then used to show the seasonal variation.

[42] Shown in Figure 11 is the seasonal distribution of characteristic vertical wavelength λ_z^*. The range of variation of λ_z^* is between 10 km and 27 km, and the annual mean is 15.8 km, values which are close to those reported by *Senft and Gardner* [1991]. There is a large variability of λ_z^* within each 10-day group, but the seasonal variation is moderately significant as u1/A1<40%. If we consider just the 6-month periods centered around the equinoxes, we get average λ_z^* values of 14.8 km in autumn and 16.8 km in spring; this 2 km difference is close to that of 2.8 km reported by *Senft and Gardner* [1991].

3.4. Temporal Frequency Spectra of the Atmospheric Density Perturbations

[43] The temporal frequency spectra Fa(ω) show the contribution of gravity waves with different frequencies to the atmospheric density perturbation:

$$F_a(\omega) = \int_{-\infty}^{\infty} B_a(0,\tau)e^{i\omega\tau}d\tau \cong \frac{\langle|R_a(z,\omega)|^2\rangle}{T} \tag{19}$$

[44] Our method for computing Fa(ω) is similar to that used by *Senft and Gardner* [1991]. However, as our photon noise is high compared to the CEDAR lidar, some data are discarded, and since the period of observations for most nights is rather short, we have to use the average of 2 adjacent nights to get reliable temporal spectra. The spatially low-pass cutoff is 1.5 km. We also enhance the high-frequency energy in the data before the spectrum is computed as in the work by *Senft and Gardner* [1991]. This method is similar to the prewhitening used in computing Fa(m).

[45] Shown in Figure 12 are four examples of the temporal frequency power spectra of the atmospheric density perturbations. The nights shown in Figure 12 are the same as those used for Figure 6. The data are scaled for temporal spectra of the density perturbations on the left-hand axis and the horizontal wind fluctuations spectra Fu(ω)

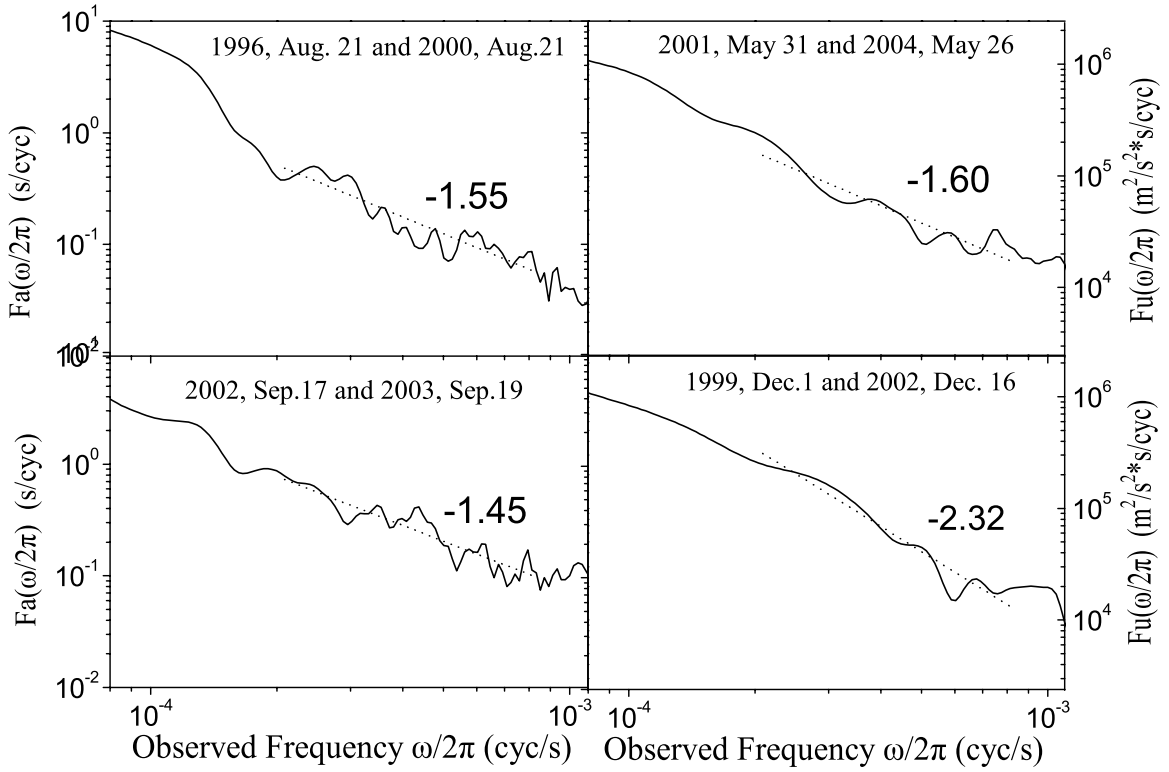

Figure 12. Four examples of the temporal frequency power spectra of the atmospheric density perturbations associated with internal gravity waves in the mesopause region. The solid curves are the temporal frequency spectra, and the dotted lines are linear regression fits to the spectra for periods from 20 to 80 min.

on the right-hand axis. Linear regression fits were adjusted to the spectra for periods from 20 to 80 min as the data time length is only 3 hours on most nights.

[46] The annual mean temporal frequency spectrum is given in Figure 13. The regression line is fitted to the spectra for periods from 20 to 80 min and the slope of the mean frequency spectrum is −1.64. The scale of the horizontal wind spectrum is also indicated on the right axis. The values of Fa(ω) ($\omega = 2\pi/1$ hour) and Fu(ω) ($\omega = 2\pi/1$ hour) are 0.6 s/cycles and 1.37×10^5 ($m^2\ s^{-2}$/(cycles/s)), respectively.

[47] Shown in Figure 14 are the annual mean temporal frequency spectra averaged over the layer topside (95–

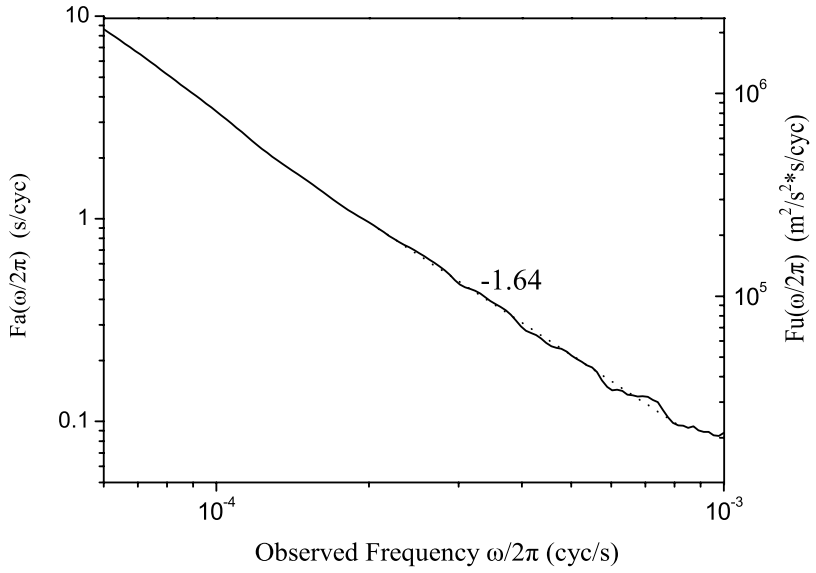

Figure 13. Temporal frequency power spectrum averaged over 82 nights of observations. The dotted lines are linear regression fits to the spectrum for periods from 20 to 80 min.

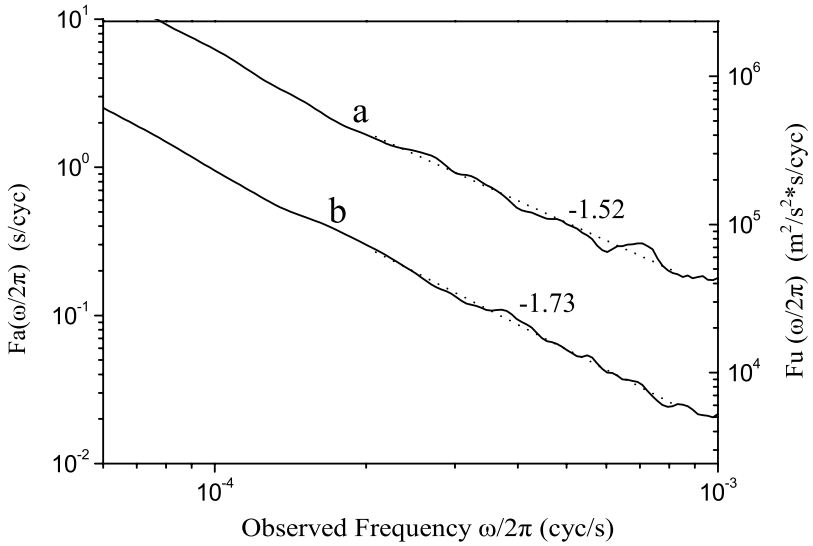

Figure 14. Annual mean temporal frequency spectra inferred from 82 lidar data sets averaged over the layer topside (95–105 km, dotted curve a) and bottomside (80–90 km, dotted curve b).

105 km) and over the bottomside (80–90 km). It can be seen from Figure 14 that the density perturbation increases with height. Fa(ω) (ω = 2π/1 hour) averaged over the topside is 7.4 times as that of the bottomside, and the corresponding growth length is 15 km.

[48] The seasonal distribution of frequency spectrum slopes (p) is shown in Figure 15, where we have plotted the two-night averages of spectral slopes fitted for periods between 20 and 80 min. The point in Figure 15 denotes the spectral slope in every two nights' average. The shallowest slope is −1.06 and the steepest is −2.32. The range of variation, 1.26, is close to the values of 1.17 obtained by *Senft and Gardner* [1991] and 1.1 obtained by *Collins et al.* [1994]. A weak seasonal variation exists as u1/A1 is 41%. The spectral slope varies greatly from day to day, in agreement with the findings of *Senft and Gardner* [1991].

[49] Shown in Figure 16 are the seasonal distributions of temporal frequency spectral amplitudes at ω_1 = 2π/60 min, ω_2 = 2π/40 min, and ω_3 = 2π/25 min. The seasonal variations of the spectral amplitudes at these three frequencies are not like that of the total density perturbation, whose maxima are near the equinoxes, and they are also unlike the

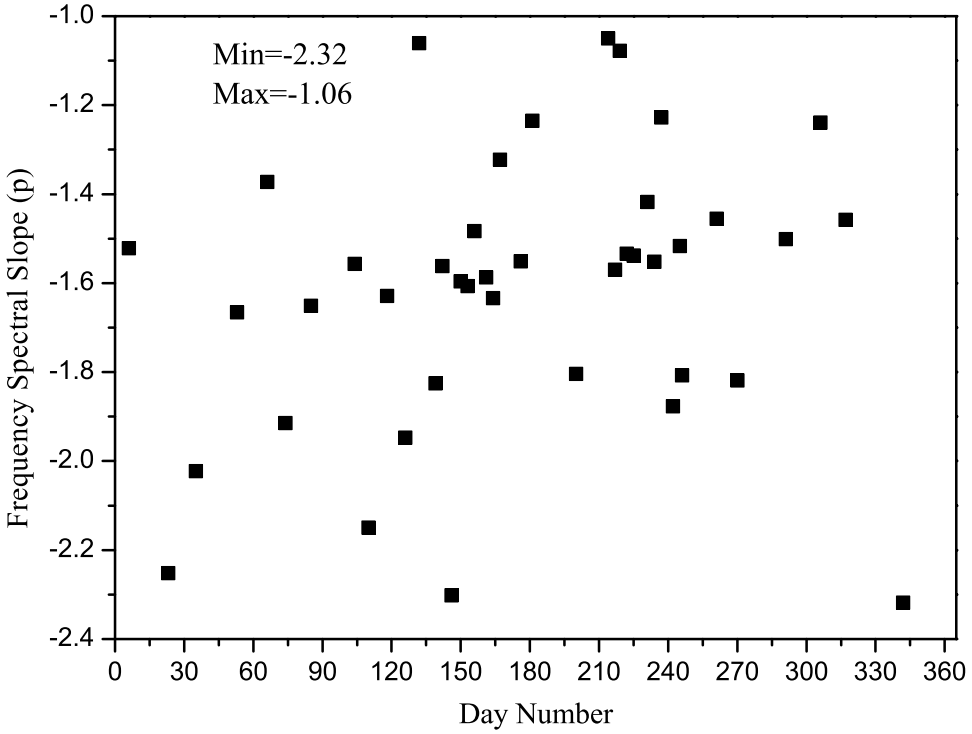

Figure 15. Seasonal distribution of the power law slopes of the temporal power spectra.

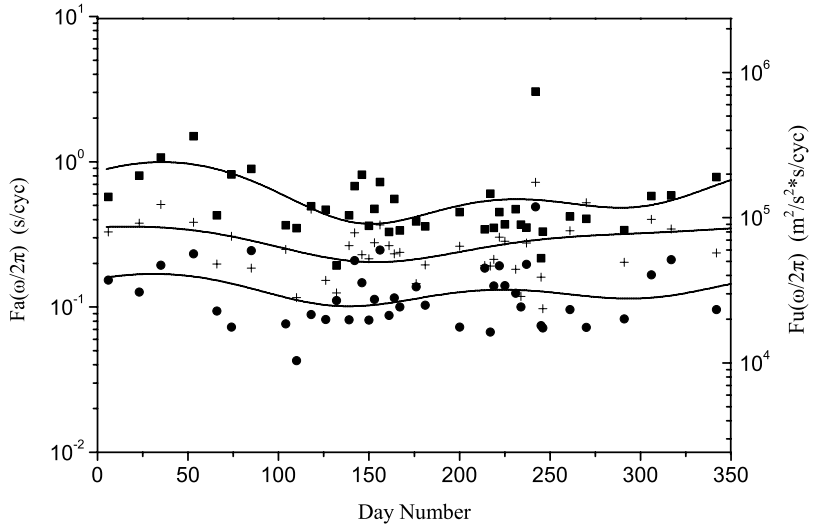

Figure 16. Seasonal distributions of temporal frequency spectral amplitudes at $\omega_1 = 2\pi/60$ min (squares), $\omega_2 = 2\pi/40$ min (pluses), and $\omega_3 = 2\pi/25$ min (circles). The solid curves are the MMSE fit for the mean, annual, and semiannual components.

results obtained by *Senft and Gardner* [1991], who found maxima around the solstices. The spectral amplitude at $\omega_1 = 2\pi/60$ min has a maximum at day 50, a minimum near day 150, and a second maximum in August. Its seasonal variation is somewhat like that of the total density perturbation or E_m, except that the amplitude in spring decreases. The spectral amplitude at $\omega_2 = 2\pi/40$ min has a maximum at day 20, and a minimum also near day 150. Its semiannual variation is very weak (2%), much smaller than the annual component (7%). The spectral amplitude at $\omega_3 = 2\pi/25$ min has two maxima at day 30 and day 220, and two minima near day 150 and day 300. Its seasonal variation is like that of the total density perturbation, but with a 50 days shift. In general, all these seasonal variations are like the total density perturbation or E_m, except the semiannual maxima is shifted to about day 40 and the annual component relatively increases.

[50] It is also possible to obtain the Characteristic temporal frequency ω^* by using the method to compute the characteristic vertical wavelength λ_z^*. The results are shown in

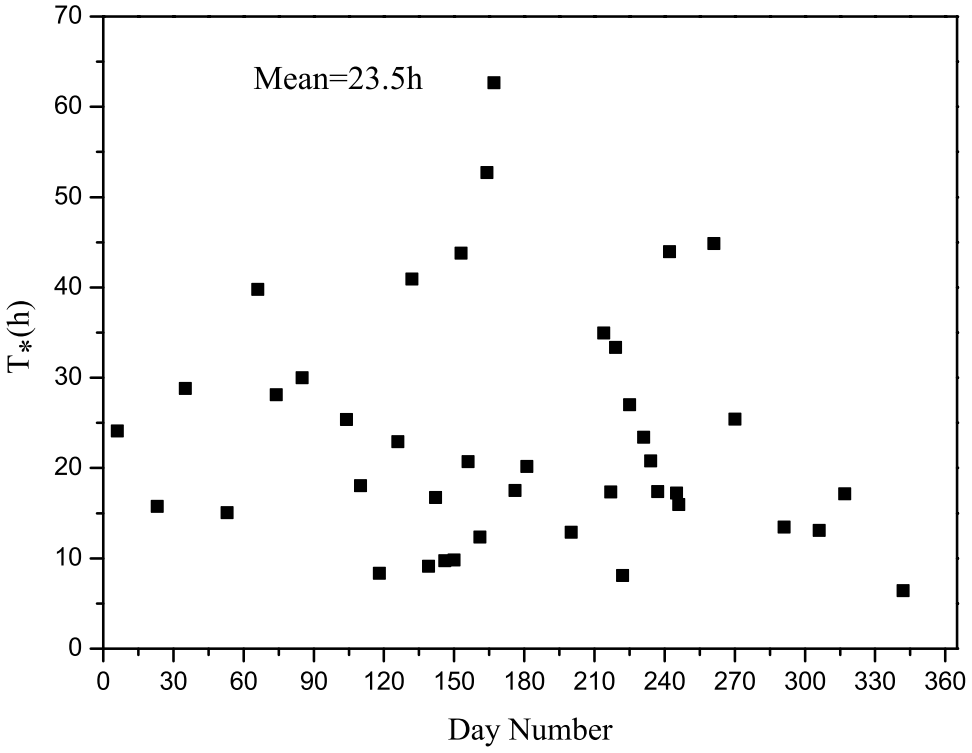

Figure 17. Seasonal distribution of characteristic periods ($T^* = 2\pi/\omega^*$).

Figure 17. It can be seen from Figure 17 that T* has a large day-to-day variability and no clear seasonal variation, as also reported by *Senft and Gardner* [1991]. The range of variation of T* is between 7 hours and 63 hours, and the annual mean is 23.5 hours. The variation range of T* is higher that of λ*. The largest values of T* (>40 hours) are not realistic because the inertial period at our site is about 31 hours. These are the artificial product of the large variations of the Fa(ω) slopes and RMS density perturbations.

4. Discussion

4.1. Comparison of Some Characteristics of the Gravity Wave Field With Other Lidar Observations

[51] The RMS atmospheric density perturbation and the RMS horizontal wind perturbations over our site are 5.1% and 25 m/s, respectively. The mean value of the RMS horizontal wind perturbations reported by *Collins et al.* [1994] is 27 m/s at South Pole. *Senft and Gardner* [1991] gave the annual mean value of the RMS horizontal wind perturbations 25 m/s at Urbana (40°N). *Beatty et al.* [1992] obtained 25 m/s at Arecibo (18°N), and *Manson et al.* [1998] obtained 24.9 m/s during ANLC-93 (40°N–55°N). Our results agree well with these lidar values. As all the lidar observations measured the same gravity wave number and frequency ranges (lower than 40 km and 4 hours), similar values of horizontal wind perturbations are to be expected. Only *Senft and Gardner* [1991] give a seasonal variation of the density perturbation and the horizontal wind perturbations. They found solstice maxima in the semiannual variation while we found maxima near the equinoxes. They found the relative semiannual and annual components of the density perturbation to be 40% and 32%, respectively, three and five times higher than ours, respectively.

[52] The annual mean density shear variance found by us is about 15 $(\%/\mathrm{km})^2$, which is much lower than that reported by *Senft and Gardner* [1991] ($37(\%/\mathrm{km})^2$) and *Senft et al.* [1993] (41 $(\%/\mathrm{km})^2$). As a consequence, the annual mean Richardson number ($\sim$1.0) found by us is also much higher than the values of 0.6 found by Senft and Gardner, and 0.63 found by Senft et al. However, Ri$\sim$1 is the conclusion from the *Dewan and Good* [1986] linear instability theory, while *Smith et al.* [1987] observed that when perturbations just reach the point of convective instability,

$$\langle \theta_z^2 \rangle / 2 = \langle (\theta_z')^2 \rangle \tag{20}$$

where Θ_z is the vertical gradient of potential temperature, which leads to

$$Ri = 2/p \tag{21}$$

where p is the spectral index of the gravity wave temporal frequency spectrum [*Gardner*, 1996]. Moreover, the diffusive filtering theory (DFT) proposed by *Gardner* [1994] also makes the assumption Ri = 1 obtained in practice. Actually, *Collins et al.* [1996], using Na wind/temperature data, also obtained at Urbana, found that the annual mean Ri is equal to 1.0, though their mean density shear variance is still twice as large as our value. From (12), we can see that Ri is proportional to N^4, which means Ri is sensitive to N. It seems this is the reason that *Senft and Gardner* [1991] obtained Ri = 0.6 assuming a fixed value for N, while *Collins et al.* [1996] obtained Ri = 1.0 at the same site with simultaneously measured value of N. As our Ri value compares well with the theoretic predication and other observations, we think the density shear variance and Richardson number measured by us are reasonable.

[53] The annual mean value of the RMS vertical wind perturbations is 0.85 m/s for our data. The value obtained by *Senft and Gardner* [1991] is 1.31 m/s, and *Senft et al.* [1993] got a high value: 2.8 m/s. Our value is lower than those reported by the other workers. A higher threshold of the filter used by us will have a small effect, but the main reason is probably the distance between gravity wave sources and the observation site. As the ratio between the horizontal and vertical distances should be proportional to u'_{rms}/w'_{rms}, and the RMS horizontal wind perturbations obtained by all the lidar observations are similar, the different distances between the source and observation site will result in different vertical wind perturbations. The main gravity wave source for *Senft and Gardner* [1991] would be the Front Range of the Rocky Mountains, which is about 1600 km from Urbana, and potential gravity wave sources are located between 800 and 1000 km from the *Senft et al.* [1993] observation site. The Andes, considered as the main gravity wave source for our data, are about 2200 km away from our site. The different source distances: 2200 km, 800 km, 1600 km, compare well with the different RMS vertical wind perturbations: 0.85 m/s, 2.8 m/s, 1.31 m/s.

[54] The mean slope of the vertical wave number spectra reported by *Senft and Gardner* [1991], was -2.90 and that reported by *Beatty et al.* [1992] was -2.98, both close to our value (-2.93). Most lidar observations report that the Fu(m) slope is near -3, which is also predicted by the linear instability theory (LIT) [*Dewan and Good*, 1986] and the Doppler-spreading theory (DST) [*Hines*, 1991]. However, *Collins et al.* [1994] reported a value of -2.4 for the slope of Fu(m) at the South Pole, and they interpret this as the inertial effect and inseparability of the (m, ω) spectrum which contribute to a steeper index in Fu(m), as the inertial frequency F at the South Pole is much higher than that at low latitudes.

[55] The magnitudes of the vertical wave number spectra in our results are comparable to those observed at other locations using lidars. The mean value of Fu(m) (m = 2π/4 km) is 3×10^5 ($m^2\ s^{-2}$/(cycles/m)) for our results. A value of 4.1×10^5 ($m^2\ s^{-2}$/(cycles/m)) was reported by *Senft and Gardner* [1991], which is 30% higher than our value. A large value, 8.7×10^5($m^2\ s^{-2}$/(cycles/m)), was reported by *Collins et al.* [1994] for the South Pole. *Beatty et al.* [1992] reported 2.9×10^5 ($m^2\ s^{-2}$/(cycles/m)) for Arecibo (18°N), which is very close to our value, consistent with the fact that their observations are for a latitude similar to ours. It seems that different sites have different Fu(m) magnitudes, and that Fu(m) increases from low to high latitudes. However, from DFT, there exists another explanation. From DFT, Fu(m) is equal to

$$Fu(m) = 2\pi \langle (u')^2 \rangle \frac{2(p-1)(s+1)}{(2p+s-1)} \frac{1}{m_*} \left(\frac{m_*}{m} \right)^{2p-1} \tag{22}$$

where p = (q + 1)/2. Assuming $\langle (u')^2 \rangle$, and s are near for all the lidar observations, the Fu(m) magnitude should be

proportional to $(q - 1)/(q + 1) \times \lambda^{*1-q}$. In addition, with the measured values of λ^* and q, we get $1200 \times (q - 1)/(q+1) \times \lambda^{*1-q}$ equal to 2.9, 3.1, 3.9, 11.9 at our site, Arecibo, Urbana, and South Pole, respectively, values comparable to the Fu(m) magnitudes ($\times 10^5 m^2 s^{-2}$/(cycles/m)): 3.0, 2.9, 4.1, 8.7 actually measured at those sites.

[56] The annual mean slope of the temporal frequency spectrum for our measurements is −1.64, which is comparable to the mean results obtained by other lidar observations (e.g., −1.85 [*Beatty et al.*, 1992], −1.74 [*Senft and Gardner*, 1991], and −1.7 [*Collins et al.*, 1994]). Unlike the Fu(m) slope, the slope of Fu(ω) is less accurately representative of the intrinsic values because of the Doppler effect of the mean wind. The variability of the observed Fu(ω) slope may reflect the variation of the Doppler effect between different sites.

[57] The magnitudes of the temporal frequency spectra derived from our observations are also comparable to those observed at other locations using lidars. We found that the annual mean value of Fu(ω) ($\omega = 2\pi/1$ h) is 1.37×10^5 ($m^2 s^{-2}$/(cycles/m)), while *Senft and Gardner* [1991] reported 2.9×10^5 ($m^2 s^{-2}$/(cycles/m)), and *Beatty et al.* [1992] obtained 1.87×10^5($m^2 s^{-2}$/(cycles/m)). A higher value 3.8×10^5 ($m^2 s^{-2}$/(cycles/m)) was obtained by *Collins et al.* [1994] at the South Pole. Again, the magnitudes increase from low latitudes to high latitudes, and this also can be explained by DFT: for all these lidar observations, the Fu(ω) magnitude is proportional to $(p - 1)f^{p-1}$. As the inertial frequency will increase from low latitudes to high latitudes, the Fu(ω) magnitude should also increase. We input the values of p and *F* (here, we use $p = (q + 1)/2$ from DFT in our results as q is more accurate and $f = 2\pi/Ti$, where Ti is the inertial period (hours)), and find $43*(p-1)f^{p-1}$ equal to: 1.38, 1.62, 3.2, 5.1 at our site, Arecibo, Urbana, and South Pole, respectively, values comparable to the measured ones of 1.37, 1.87, 2.9, and 3.8($\times 10^5$ ($m^2 s^{-2}$/(cycles/m)).

[58] The characteristic vertical wave number of the gravity wave field, m*, defines the breakpoint between the weak and strong wave interaction subranges. When wave number m is lower than m*, there is little wave interaction and the vertical wave number spectrum is influenced primarily by the sources. When m is larger than m*, the spectrum is controlled by the saturation and dissipation processes. The annual mean characteristic wavelength $\lambda^* = 2\pi/m^*$ reported by *Senft and Gardner* [1991] for the mesopause region was 14.1 km, which is close to our annual mean value 15.8 km. Similar results for λ^*, reported by other lidar observations are 14.3 km [*Senft et al.*, 1993], 14.2 km [*Collins et al.*, 1994], and 11.7 km [*Manson et al.*, 1998]. DST proposed by *Hines* [1991] suggested that the characteristic wavelength is proportional to the gravity wave RMS velocity,

$$\lambda_* = 2T_B u_{rms} \tag{23}$$

and LIT and DFT also indicate that: $\lambda^* \sim u_{rms}/N$. As u_{rms} obtained by all the lidar observations are approximate the same, the characteristic wavelength λ^* obtained by us is close to other lidar results. Moreover, from (32), we can obtain that λ^* is 16 km, which is close to our annual mean value 15.8 km.

[59] The characteristic temporal frequency ω^* is an analogous parameter for the density spectra. The characteristic period $T^* = 2\pi/\omega^*$ may be regarded as the period of the dominant gravity wave associated with λ^*. Because the gravity wave intrinsic spectrum has a low-frequency cutoff at the inertial frequency f, ω^* is probably closely related to f. The annual mean T* reported by *Senft and Gardner* [1991] is 9.7 hours, which is much lower than our value of 23.5 hours. As the inertial period at our site is about 31 hours, which is much higher than that at Urbana (19 hours), it is not surprising that our T* is much higher than the Illinois value. Also, the value of $T^* \sim 20$ hours reported by *Senft et al.* [1993] for Arecibo also a low-latitude site, is consistent with our result, as their inertial period is ~39 hours.

4.2. Seasonal Variation of the Gravity Wave Activity in the Mesopause Region

[60] From the measured results, we conclude that the maxima of the density perturbation induced by gravity waves with longer wavelengths occur near the equinoxes, but this seasonal variation will change for gravity waves with shorter periods or wavelengths, with the relative amplitude of the annual component increasing and the semiannual maximum shifting to day 40. As the energy of gravity waves with longer wavelengths is much larger than that for shorter wavelength gravity waves, and the density perturbation is mainly induced by the gravity waves with longer wavelengths, then as the maxima in the total perturbation and the variance for fluctuations with vertical scales between 2 and 10 km occur near the equinoxes, we believe that the maxima of the gravity wave activity also occur near the equinoxes over our site.

[61] There are many observations of the seasonal variation of the gravity wave activity in the middle atmosphere. Throughout the stratosphere, from polar region to lower latitudes the observations show an annual maximum in winter and minimum in summer: polar region, [*Yoshiki and Sato*, 2000], 44°N [*Whiteway and Carswell*, 1995], 35°N [*Tsuda et al.*, 1994], and over Japan [*Kitamura and Hirota*, 1989]. However, some observations at low south latitudes show a wave activity maximum in southern summer [*Allen and Vincent*, 1995; *Vincent and Alexander*, 2000]. In the mesosphere (65–85 km) observations, the solstice maximum is also present, but the semiannual component is dominant instead of the annual [*Vincent and Fritts*, 1987; *Tsuda et al.*, 1994]. To compare the sodium lidar observations, we only discuss the seasonal variation of the gravity wave activity in the mesopause region. At middle and high latitudes (40°N and and 65°) using lidar [*Senft and Gardner* [1991] and MST radar [*Balsley et al.*, 1983] and at 67°S using MF radar [*Vincent*, 1994], all authors report that the maxima of the gravity wave seasonal variation occur near the solstices. *Gavrilov and Jacobi* [2004] using LF D1 wind observations data from Collm, Germany (52°N, 15°E) found that the gravity wave perturbations maxima occur at the solstices near 83 km, but they shift to the equinoxes near and above 100 km. At lower latitudes, *Reisin and Scheer* [2004] report that the maxima in gravity wave activity (from 87 km to 95 km) occur at the solstices, using airglow data from E1 Leoncito (31.8°S, 69.2°W). However, on the basis of MF radar data from Hawaii (22°N, 160°W), *Gavrilov et al.* [2003] found semiannual maxima in gravity wave intensity at the solstices below 83 km, shifting to the equinoxes at higher

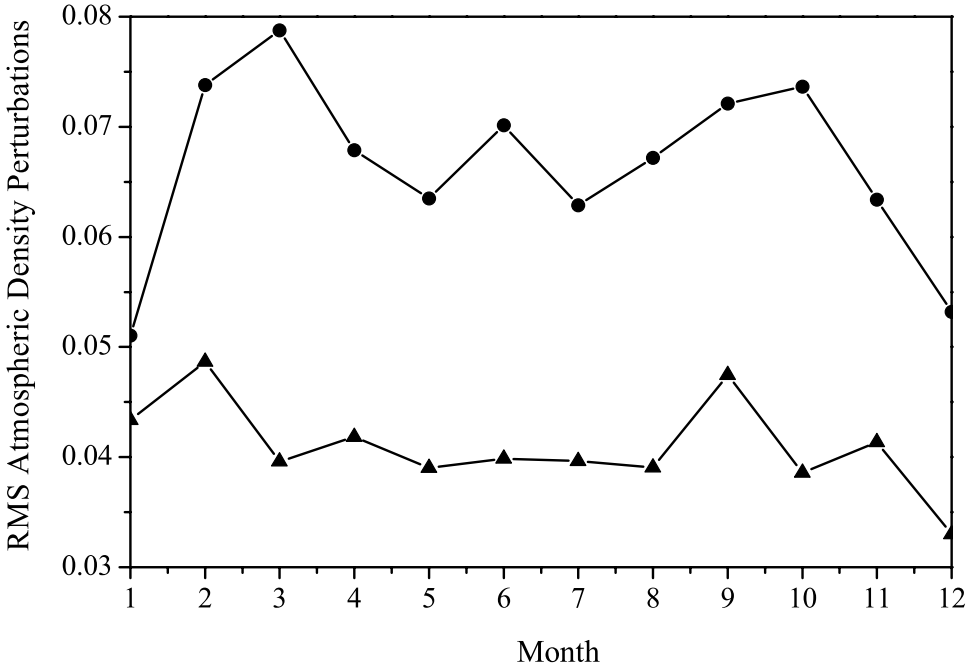

Figure 18. Monthly average density perturbations for two altitude regions: triangles, 80–90 km and circles, 92–101 km.

altitudes. From Figure 2, we can see that the density perturbations we observe at the bottom of the sodium layer do not vary much with season, but increase with height more in spring and autumn than in summer and winter. This can be seen clearly from Figure 18, where we show monthly average RMS atmospheric density perturbations for two altitude regions, 80–90 km and 92–101 km. The density perturbation does not present any obvious seasonal variation at the bottom of the sodium layer, but the more rapid growth with height at the equinoxes leads to equinoctial maxima in the 92–101 km region. This result is similar to that reported by *Gavrilov et al.* [2003].

[62] *Gavrilov and Fukao* [1999] use a model to explain the summer maximum of gravity wave amplitude in the mesosphere. From their model, they find that the eastward propagating gravity waves in the troposphere suffer less dissipation in the stratosphere in summer because the stratospheric winds in summer are westward. So the gravity wave amplitude in summer is a maximum in the mesosphere (~70 km), although it is a minimum in the upper troposphere. Moreover, we note that their model also predicts that the maxima in gravity wave amplitude occur near the equinoxes, rather than solstices, at higher altitude – 100 km [*Gavrilov and Fukao*, 1999, Figures 3, 5, and 6]. Under their explanation, we can think this as the result of the fact that the eastward propagating gravity waves will suffer more dissipation as the mean winds at 80–100 km change back to eastward propagation in summer. From the structure of the mean winds in the meteor region reported by *Batista et al.* [2004] for our location, we can see that the high-speed zonal winds will change their propagation direction above 90 km in winter, and that the speed is also very high at the inverse direction. So in winter, the surviving gravity waves traveling opposite to the mean flow below 90 km will suffer more dissipation as the mean wind changes its propagation direction above 90 km, and the same situation will also be present in summer, helping the formation of equinoctial maxima over our site. *Gavrilov et al.* [2003] attributed the shift in the maxima of the gravity wave intensity to the equinoxes at altitudes higher than ~83 km to the dependence of gravity wave generation and propagation on the background wind and temperature. However, we can see from their model result [*Gavrilov et al.*, 2003, Figure 15] that the gravity wave intensity will decrease greatly between 80 km and 90 km in summer, and at this time of the year, the high-speed zonal wind in the middle atmosphere will change its propagation direction above 80 km, where the speed is also very high at the inverse direction [*Gavrilov et al.*, 2003, Figure 14]. This situation is similar to that over our site in winter, when the greater dissipation above 90 km may limit gravity wave amplitudes, leading to minima in height-integrated gravity wave activity at the solstices.

4.3. Comparison With Theories of Gravity Wave Saturation and Dissipation

[63] The slope of the vertical wave number spectrum varies greatly from night to night, which is not caused by the photon noise bias, as the relative RMS error of the photon noise bias is less than 13%. This large variability, which is also reported by other lidar observations, is not compatible with LIT. LIT suggests that the spectrum goes as m^{-3} if the bandwidth of a wave packet is proportional to m. So the bandwidth of a wave packet must be proportional to m^{q-2}, if the slope q is not equal to 3. In our result (Figure 8), the bandwidth dependence ranges from $m^{0.06}$ to $m^{1.81}$ and changes dramatically from night to night. These extreme night-to-night changes are unreasonable.

[64] As pointed out by *Senft and Gardner* [1991], the observed slope variability appears to be compatible with

Table 3. Measured Gravity Wave Parameters Compared to DFT Predication

Parameter	Measured	Predicted (p = 1.972, s = 1, Ri = 1)
$\langle(u')^2\rangle$, m^2/s^2	$(25)^2$	
λ_z^*, km	15.8	12.9
Fu(m) slope	2.93	2.93
Fu(m)@2π/4 km, (10^5 m^2/s^2)/(cycles/m)	3.0	2.6
Fu(ω) slope	1.64	1.972
Fu(ω)@2π/1 hour,(m^2/s^2)/(cycles/s)	1.37	0.79

DST. The slope predicted by Hines theory depends on the high wave number cutoff of the source spectrum, and the slope variability may be caused by night-to-night changes in the source spectrum cutoff. The observed slope variability is also compatible with DFT. DFT suggests that a wave of intrinsic frequency ω_i and vertical wave number m will be severely damped when the effective vertical diffusion velocity (mD_{zz}) of particles experiencing the wave motion exceeds the vertical phase velocity of the wave (ω/m). Thus only waves satisfying $mD_{zz} \leq \omega/m$ are permitted to grow in amplitude with increasing altitude. The variability of the vertical wave number spectrum slope can be attributed to the variability of the source spectrum slope under DFT.

[65] DFT, proposed by *Gardner* [1994], gives the detailed formulas to calculate the gravity wave parameters *Gardner* [1994, Table 2], and we use these formulas to calculate the gravity wave parameters and compare them to our measured values. The results are listed in Table 3. From Table 3, we can see that predicated parameter values are comparable to the measured values except the Fu(ω) slope. The predicated magnitude of Fu(ω) is 50% less than the measured magnitude, which may be the result of Doppler shifting caused by the background wind field enhancing the magnitude of Fu(ω) at high frequencies [*Gardner*, 1994]. We found the correlation coefficient between the seasonal distributions of q (the data points in Figure 8) and p (the data points in Figure 15) is 0.05, which means that p is not correlated to q. However, from DFT, p and q are correlated to the source and have systematic relationship. Moreover, the annual mean p is -1.64, which is not -1.97 as DFT predicated, and *Gardner* [1994, p. 20,616] indicated that "The combined effects of Doppler shifting by the background wind field and data filtering may have obscured the relationships between the spectral slopes."

[66] The values of B_{rms} and m_{rms} ω_{rms} in our results are lower than those obtained by *Senft and Gardner* [1991] as thresholds of our cutoffs are higher, but our results indicate that the joint (m,ω) spectrum is not separable when m and ω are lower than the thresholds. This is also not compatible with the linear instability theory, as separability is a direct mathematical consequence of the physical mechanisms that control energy dissipation in linear instability theory. However, our results are compatible with DFT, while DFT predicts that the joint (m, ω) spectrum is not separable because the cutoff condition $\omega = m^2D_{zz}$ depends on m and ω. However, because of the Doppler effects, the observed frequency ω is not the intrinsic ω of the gravity wave, and this will have an effect on the test of the separability of the joint (m, ω) spectrum.

5. Conclusions

[67] We have measured the seasonal variation of gravity wave activity at 23°S, and find that the maxima occur near the equinoxes. The total density perturbation, the density variance for fluctuations with 2 km to 10 km, and the vertical wave number spectral amplitudes at 2π/(8 km) and 2π/(4 km) all show that the semiannual maxima occur near the equinoxes, although the short-scale waves show some divergence from this behavior. This result is different to that observed at higher latitudes, where the maxima of the gravity wave activity occur near the solstices. However, it is similar to that reported by *Gavrilov et al.* [2003] at another low-latitude site (Hawaii, 22°N), and at both sites it is found that the maximum gravity wave activity occurs near the equinoxes only at higher altitudes, an effect which may be produced by the background wind influencing the gravity wave propagation and dissipation.

[68] We determined the seasonal variations of a number of characteristics of the gravity wave field. The annual mean value of RMS atmospheric density perturbation and the RMS horizontal wind perturbations are 5.1% and 25 m/s, respectively, with maxima in March. The annual mean growth length of the density perturbations is 38 km, and the growth lengths in spring and autumn are lower than those in summer and winter. The annual mean density shear variance is about 15 $(\%/km)^2$ and the mean Richardson number is about 1.0. The maxima of the Richardson number occur near solstices and the range of variation is from 0.5 to 2. The mean value of the RMS vertical wind perturbations is 0.85 m/s with the annual maximum occurring at the end of the year. The nightly average slope of the vertical wave number spectrum Fa(m) varies between -2.06 and -3.81, and the annual mean value is -2.93. The amplitudes of Fa(m) (m = 2π/4 km) and of Fu(m) (m = 2π/4 km) are 1.35(m/cycles) and $3*10^5$(m^2 s^{-2}/(cycles/m)), respectively, with semiannual maxima occurring near the equinoxes. The range of variation of λ_z^* is between 10 km and 27 km, and the annual mean is 15.8 km, which is consistent with *Hines*' [1991] DST predication. The value of λ_z^* averaged around autumn equinox is 14.8 km, which is lower than the value 16.8 km averaged around spring equinox. The range of variation of the temporal frequency spectral slope is between -1.06 and -2.32, and the annual mean value is -1.64. The annual mean values of Fa(ω) (ω = 2π/1 hour) and Fu(ω) (ω = 2π/1 hour) are 0.6(s/cycle) and 1.37×10^5 (m^2 s^{-2}/(cycles/s), respectively, with the maximum occurring near day 50. The range of variation of T* is from 7 hours to 63 hours, and the annual mean is 23.5 hours. All of the above parameters exhibit large nightly variability, and most of them exhibit seasonal variation. The characteristics of the gravity wave field determined from our measurements are comparable to other observations using lidar, and most differences can be explained by the wave dissipation and saturation theories in conjunction with latitudinal differences.

[69] Our results are not compatible with the linear instability theory, as we found that the slopes of the vertical wave number spectra vary greatly from night to night and the joint (m, ω) spectrum is not separable. However, these

results are compatible with the Hines Doppler-spreading theory and the Gardner diffusive filtering theory.

[70] We do not have regular measurements of the relevant temperature profile, so we have to use a fixed value of the Brunt-Vaisala frequency based on a limited number of measurements, and this might affect the estimates for the horizontal wind perturbations and their spectra, as N would also be expected to have a seasonal variation. However, we are in the process of installing a sodium temperature lidar at our site, which will enable us make temperature profile measurements simultaneously with the gravity wave observations, allowing us to make more accurate estimates of gravity wave parameters and better comparisons with theories of gravity wave saturation and dissipation.

[71] **Acknowledgment.** This work has been supported by the Fundação de Apoio a Pesquisa do Estado de São Paulo, and the Conselho Nacional de Desenvolvimento Científico e Tecnológico.

References

Allen, S. J., and R. A. Vincent (1995), Gravity wave activity in the lower atmosphere: Seasonal and latitudinal variations, *J. Geophys. Res.*, *100*, 1327–1350.

Balsley, B. B., W. L. Ecklund, and D. C. Fritts (1983), VHF echoes from the high-latitude mesosphere and lower thermosphere: Observations and interpretations, *J. Atmos. Sci.*, *40*, 2451–2466.

Batista, P. P., B. R. Clemesha, I. S. Batista, and D. M. Simonich (1989), Characteristics of the sporadic sodium layers observed at 23°S, *J. Geophys. Res.*, *94*, 15,349–15,358.

Batista, P. P., B. R. Clemesha, A. S. Tokumoto, and L. M. Lima (2004), Structure of the mean winds and tides in the meteor region over Cachoeira Paulista, Brazil (22.7°S, 45°W) and its comparison with models, *J. Atmos. Sol. Terr. Phys.*, *66*, 623–636.

Beatty, T. J., C. A. Hostetler, and C. S. Gardner (1992), Lidar observations of gravity wave and their spectra near the mesopause and stratopause at Arecibo, *J. Atmos. Sci.*, *49*, 477–496.

Clemesha, B. R., D. M. Simonich, and P. P. Batista (1992), A long-term trend in the height of the atmospheric sodium layer: Possible evidence for global change, *Geophys. Res. Lett.*, *19*, 457–460.

Clemesha, B. R., I. Veselovskii, P. P. Batista, M. P. P. M. Jorge, and D. M. Simonich (1999), First mesopause temperature profiles from a fixed southern hemisphere site, *Geophys. Res. Lett.*, *26*, 1681–1684.

Collins, R. L., A. Nomura, and C. S. Gardner (1994), Gravity waves in the upper mesosphere over Antarctica: Lidar observations at the South Pole and Syowa, *J. Geophys. Res.*, *99*, 5475–5485.

Collins, R. L., X. Tao, and C. S. Gardner (1996), Gravity wave activity in the upper mesosphere over Urbana, Illinois: Lidar observations and analysis of gravity wave propagation models, *J. Atmos. Terr. Phys.*, *58*, 1905–1926.

Dewan, E. M. (1994), The saturated-cascade model for atmospheric gravity wave spectra, and the wavelength-period (W-P) relations, *Geophys. Res. Lett.*, *21*, 817–820.

Dewan, E. M., and R. E. Good (1986), Saturation and the ''universal spectrum for vertical profiles of horizontal scalar winds in the atmosphere, *J. Geophys. Res.*, *91*, 2742–2748.

Fritts, D. C., and M. J. Alexander (2003), Gravity wave dynamics and effects in the middle atmosphere, *Rev. Geophys.*, *41*(1), 1003, doi:10.1029/2001RG000106.

Gardner, C. S. (1994), Diffusive filtering theory of gravity wave spectra in the atmosphere, *J. Geophys. Res.*, *99*, 20,601–20,622.

Gardner, C. S. (1996), Testing theories of atmospheric gravity wave saturation and dissipation, *J. Atmos. Terr. Phys.*, *58*, 1575–1589.

Gavrilov, N. M., and S. Fukao (1999), A comparison of seasonal variations of gravity wave intensity observed by the MU radar with a theoretical model, *J. Atmos. Sci.*, *56*, 3485–3494.

Gavrilov, N. M., and C. Jacobi (2004), A study of seasonal variations of gravity wave intensity in the lower thermosphere using LF D1 wind observations and a numerical model, *Ann. Geophys.*, *22*, 35–45.

Gavrilov, N. M., D. M. Riggin, and D. C. Fritts (2003), Medium-frequency radar studies of gravity-wave seasonal variations over Hawaii (22°N, 160°W), *J. Geophys. Res.*, *108*(D20), 4655, doi:10.1029/2002JD003131.

Hines, C. O. (1991), The saturation of gravity waves in the middle atmosphere, part [22]. Development of Doppler-spread theory, *J. Atmos. Sci.*, *48*, 1360–1379.

Kitamura, Y., and I. Hirota (1989), Small-scale disturbance in the lower stratosphere revealed by daily rawin sonde observations, *J. Meteorol. Soc. Jpn.*, *67*, 817–830.

Manson, A. H., C. E. Meek, J. Qian, and C. S. Gardner (1998), Spectra of gravity wave density and wind perturbations observed during Artic Noctilucent Cloud (ANLC-93) campaign over the Canadian Prairies: Synergistic airborne Na lidar and MF radar observations, *J. Geophys. Res.*, *103*, 6455–6465.

Reisin, E. R., and J. J. Scheer (2004), Gravity wave activity in the mesopause region from airglow measurements at EI Leoncito, *J. Atmos. Sol. Terr. Phys.*, *66*, 655–661.

Senft, D. C., and C. S. Gardner (1991), Seasonal variability of gravity wave activity and spectra in the mesopause region at Urbana, *J. Geophys. Res.*, *96*, 17,229–17,264.

Senft, D. C., C. A. Hostetler, and C. S. Gardner (1993), Characteristics of gravity wave activity and spectra in the upper stratosphere and upper mesosphere at Arecibo during early April 1989, *J. Atmos. Terr. Phys.*, *55*, 425–439.

Simonich, D. M., B. R. Clemesha, and V. W. J. H. Kirchhoff (1979), The mesospheric sodium layer at 23°S: Nocturnal and seasonal variations, *J. Geophys. Res.*, *84*, 1543–1550.

Smith, S. A., D. C. Fritts, and T. E. Vanzandt (1987), Evidence for a saturated spectrum of atmospheric gravity waves, *J. Atmos. Sci.*, *44*, 1404–1410.

Tsuda, T., T. Inoue, D. C. Fritts, T. E. Vanzandt, S. Kato, T. Sato, and S. Fukao (1989), MST radar observations of a saturated gravity wave spectrum, *J. Atmos. Sci.*, *46*, 2440–2447.

Tsuda, T., Y. Murayama, T. Nakamura, R. A. Vincent, A. H. Manson, C. E. Meek, and R. L. Wilson (1994), Variations of the gravity wave characteristics with height, season and latitude revealed by comparative observations, *J. Atmos. Terr. Phys.*, *56*, 555–568.

Vanzandt, T. E. (1982), A universal spectrum of buoyancy waves in the atmosphere, *Geophys. Res. Lett.*, *9*, 575–578.

Vincent, R. A. (1994), Gravity-wave motions in the mesosphere and lower thermosphere observed at Mawson, Antarctica, *J. Atmos. Terr. Phys.*, *56*, 593–602.

Vincent, R. A., and M. J. Alexander (2000), Gravity waves in the tropical lower stratosphere: An observational study of seasonal and interannual variability, *J. Geophys. Res.*, *105*, 17,971–17,982.

Vincent, R. A., and D. C. Fritts (1987), A climatology of gravity wave motions in the mesopause region at Adelaide, Australia, *J. Atmos. Sci.*, *44*, 748–760.

Whiteway, J. A., and A. I. Carswell (1995), Lidar observations of gravity wave activity in the upper stratosphere over Toronto, *J. Geophys. Res.*, *100*, 14,113–14,124.

Yoshiki, M., and K. Sato (2000), A statistical study of gravity waves in the polar regions based on operational radiosonde data, *J. Geophys. Res.*, *105*, 17,995–18,012.

P. Batista, B. Clemesha, D. Simonich, and G. Yang, Instituto Nacional de Pesquisas Espaciais, São José dos Campos, 23337-010 SP, Brazil. (bclem@laser.inpe.br)